# *Observed and modeled urban heat island and sea breeze circulation interactions: a Shanghai case study*

Article

Accepted Version

# Observed and Modeled Urban Heat Island and Sea Breeze Circulation Interactions: a Shanghai Case Study

Yan HU[1], Jianguo TAN[2*], Sue Grimmond[3], Xiangyu AO[1], Yafei YAN[4], Dongwei LIU[1]

*[1] Shanghai Ecological Forecasting and Remote Sensing Center, Shanghai Meteorological Service, Shanghai 200030, China [2] Key Laboratory of Cities' Mitigation and Adaptation to Climate Change in Shanghai (CMACC), Shanghai Climate Center, Shanghai Meteorological Service, Shanghai [3] Department of Meteorology, University of Reading, UK [4] School of Environmental and Geographical Sciences (SEGS), Shanghai Normal University, Shanghai, China * jianguot@21cn.com*

ABSTRACT

Urban heat island (UHI) and sea-land breeze systems are well-known and important characteristics of the climate of coastal cities. To model these, the accurate estimation of the surface energy balance (SEB) is a key factor needed to improve local scale simulations of thermodynamic and dynamic boundary circulations. The Weather Research and Forecasting model with a single layer urban model (WRF/SLUCM), with parameters derived from MODIS and local GIS information, is used to investigate the UHI and sea breeze circulations (SBC) in the megacity of Shanghai. The WRF/SLUCM can reproduce observed urban radiation and SEB fluxes, near-surface meteorological variables, and the evolution of the UHI and SBC. Simulations for an August period show the maximum UHI tends to drift northwest in the afternoon, driven by the prevailing southeast wind. The sea breeze lasts for about 4-h and is strongest between 1200 and 1400 Local Time (UTC+8 h). The interaction between UHI and SBC is evident with low-level convergence, upward motion and moisture transport from the sea and urban breezes simulated. An urban circulation (horizontal/vertical/time scales: ~20-km/ ~1.5-km/ ~3-h) with thermal vertical motions (~1.5 m $s^{-1}$) above the urban area and a SBC (horizontal/vertical/time scales: 6 - 7 km/ ~1 km/ 2 - 3-h) above the northern coastal suburb occur. Combined the sea breeze and southerly winds form a low-level wind shear (convergence zone) ~5 km from the coast that penetrates ~20 km inland to the urban center. Using the WRF/SLUCM simulations we improve understanding of the complex spatial dynamics of summer-time urban heating in coastal megacities, such as Shanghai.

## 1. Introduction

Globally many people live in major coastal cities, where both urban heat island (UHI) and sea-land breeze circulation (SBC) systems occur, and can have important influences on the climate. In urban areas, buildings and roads have high heat capacities (Ek et al. 2003), while areas with less vegetation often have reduced soil moisture lowering the latent heat flux ($Q_E$). Urban form enhances shadowing, increases surface roughness, modifies canopy layer radiative exchanges and absorption and turbulent exchanges. Cities also have additional emissions of anthropogenic heat ($Q_F$). These differences of radiative, thermal, and dynamic properties in urban areas modify the surface energy balance (SEB) and boundary layer structure in and near cities local UHI circulation systems (Oke et al. 2017). Some of the largest observed canopy layer-UHI (CL-UHI) are recorded in summertime under clear sky, low wind, 2-3 h after sunset conditions (Oke 1981; Oke et al. 2017) when the rural and urban areas are exposed to the same climate. However, for numerous reasons other patterns occur (WMO 2021), including: (1) averaging over longer periods with different synoptic conditions within one season or longer, (2) urban and rural areas are not exposed to the same regional climate (i.e., combined effects – not just urban processes), and (3) in winter the role of anthropogenic heat flux emissions may play an important role in some regions.

The mesoscale SBC, occurring at many coastal locations globally, develops from differential heating between land and water. This allows temperature differences to create a mesoscale pressure gradient force towards the land (Miller et al. 2003). In addition, the land surface sensible heat flux, ambient geostrophic wind, atmospheric stability, atmospheric moisture, water body dimensions, terrain height, terrain slope, Coriolis parameter, surface aerodynamic roughness length, and shoreline curvature can influence the development and evolution of SBCs (Crosman and Horel 2010). The depth of the sea-breeze gravity current as it passes over heated land surface deepens nonlinearly with increasing distance inland due to boundary-layer convection (Garratt et al. 1990; Miller et al. 2003). Particularly when a SBC develops near a coastal city, it may be modified (Yoshikado 1990, 1992) through interactions with both the UHI circulation (e.g., frictional retardation, thermal coupling) and geography (e.g., extent of urban area, distance of the urban area to the coast and surrounding topography; Ohashi and Kida 2002), thus potentially affecting the sea breeze both thermo-dynamically and aerodynamically (Varquez et al. 2015). The intensity of the UHI and building roughness may strengthen or weaken the sea breeze.

UHI and SBC systems have been investigated in numerous costal urban areas globally (e.g., Brazil: São Paulo - Freitas et al. 2007; Canada: Vancouver - Leroyer et al. 2014; China: Hong Kong - Wang et al. 2017, Pearl River Delta Region - You et al. 2019; Greece: Athens - Dandou et al. 2009; Japan : Osaka, Kyoto and Tokyo - Ohashi and Kida 2002; South Korea: Seoul - Ryu and Baik 2013; USA: Houston - Cheng and Byun 2008, Chen et al. 2011b, New York city - Childs and Raman 2005, Thompson et al. 2007). The studies have included use of observations (e.g., Childs and Raman 2005) and mesoscale modelling (e.g., ARPS: Childs and Raman 2005; MM5: Dandou et al. 2009; RAMS/TEB: Freitas et al. 2007; WRF-BEP-BEM: Wang et al. 2017; WRF/UCM: Chen et al. 2011a, b). The role of mountains (e.g., Ohashi and Kida 2002) and UHIs (e.g., Childs and Raman 2005; Freitas et al. 2007; Cheng and Byun 2008) impacts on the SBC for stagnation points (e.g., Ohashi and Kida 2002; Chen et al. 2011b) or penetration distance (e.g., You et al. 2019) and dispersion (e.g., Thompson et al. 2007) have been explored. However, many studies rely only on numerical models, but lack long-term observations (e.g. high-quality surface flux, and dense automated surface observing systems (ASOS)) to verify the urban SEB, UHIs, and SBCs. Neither the evolution of UHI circulation under the influence of sea breeze nor the development of the urban sea breeze and the structure of the affected urban boundary layer have been explored fully.

Our objectives are: (1) to derive appropriate surface parameters to simulate near surface and boundary layer atmospheric conditions; (2) to evaluate simulations using observations; and (3) to analyze the interactions between the summer UHI and SBC with a typical UHI and sea breeze case.

This research, is undertaken in Shanghai, as there is a dense meteorological network (Tan et al. 2015) and long term urban surface energy balance flux measurement site (Ao et al. 2016). Shanghai is one of the largest and most densely populated cities in the world. Given its location on the East China coast, the SBC is an important influence on this region. The large urban extent is associated with a well-developed UHI.

We use the Weather Research and Forecasting (WRF) numerical weather prediction (NWP) model. To parameterize the sub-grid scale processes, including the complexity and heterogeneity of the urban surface atmosphere exchanges, one of the many coupled urban canopy models (UCMs) needs to be selected but the results are sensitive to the choice both of the model and parameter values (e.g., Miao et al. 2009; Loridan et al. 2010, 2013; Salamanca et al. 2011; Li et al. 2013a, b, 2015b). The UCMs vary in complexity, assumptions, computing time, and model parameters from the relatively simple with minimal data requirements or computer needs (e.g., slab) to more complex assumptions about the processes but with greater demands on surface parameters and computer resources (e.g., multi-layer; Chen et al. 2011a). The accuracy of modelled SEB fluxes requires the urban surface parameters to be correct (Loridan et al. 2010; Wang et al. 2011; Grimmond et al. 2010, 2011; Zhao et al. 2014a) but assigning these required parameters remains challenging (Tsiringakis et al. 2019). Additionally, the correct prescription of these properties may be as important as the complexity of the UCMs used to parametrize the physical processes (Grimmond et al. 2011; Best and Grimmond 2015). Hence, our first objective addresses deriving these parameters for the single layer UCM (Kusaka et al. 2001) for Shanghai. This is a medium complexity urban land surface model (Grimmond et al. 2010, 2011; Chen et al. 2011) with the compromise between model physics and parameter needs.

With the appropriate model parameters chosen, the model is used to improve understanding on the interaction between UHI and SBC, specifically of the evolution of UHI circulation under the influence of sea breeze; and the development of the urban sea breeze and the structure of the affected urban boundary layer. This also use the extensive array of sensors located across the study area (Tan et al. 2015) allowing analysis of these dynamics, using not only numerically modelling but also observations.

## 2. Data and Methods

The Shanghai megalopolis is the focus of our investigation of summertime interactions between UHI and SBC. Analysis of this coastal urban area, aids understanding in subtropical urban climates but also in the delivery of integrated urban services (Grimmond et al. 2020). This type of urban area is expected to grow and be home to more, potentially vulnerable, people in the near future.

### *2.1 Study area and climatology*

Shanghai, located south of the Yangtze River estuary between Jiangsu and Zhejiang Provinces, the East China Sea and Hangzhou Bay (Fig. 1), has very flat topography with mean altitude about 4 m (2-103 m) above sea level. The local climate zones (LCZ, Stewart and Oke 2012) where observations are undertaken include (Fig 1b): LCZ 1: compact high-rise (central business district: XJH), LCZ 5: open mid-rise (suburban: JD), and LCZ 6: open low-rise (exurban sites: CM, FX, JS, SJ).

The UHI and SBC are both major influences on Shanghai's climate, especially in summer. The UHI structure is irregular owing to the heterogeneity of underlying surface. However, this is based on limited knowledge of the CL-UHI, as previous studies have used the 2 m air temperature from only two sites (urban: XJH and exurban: e.g., FX) (e.g., Shen et al. 2020). Using these two sites, CL-UHI is observed to have increased in size between 1987 and 2004 but decreased more recently (2005–2017). In this period, the land cover and building density changed in both areas. The central city area (XJH) has changed from open high-rise (LCZ 4) to compact high-rise (LCZ 1) and in the 'rural' reference (FX) it changed from sparsely built (LCZ 9) to open low-rise (LCZ 6).

In summer, the peak CL-UHI in Shanghai occurs at 1400 LST (Local Standard Time= UTC+8 h; Tan et al. 2010; Ao et al. 2019a, b) rather the more widely documented 2-3-h after sunset (e.g., Baltimore–Washington: Li and Bou-Zeid 2013c; Beijing: Li et al. 2016, 2017). A wide range factors can influence the timing of UHI peak, including local climate background, city geographical setting and soil moisture, *etc*. (Zhao et al. 2014b, Dou et al. 2015). The soil moisture content controls when an UHI forms and it magnitude (e.g. Grimmond et al. 1993, Zhao et al. 2014b). The daily peak intensity of the Shanghai CL-UHI in summer (JJA, 2005–2007; urban XJH relative to four exurban sites: CM, FX, JS, SJ) is in the range of 0.5-2.0°C (Tan et al. 2010). It typically occurs between noon and early afternoon, corresponding approximately with the daily maximum air temperature (Tan et al. 2010).

Coastal Shanghai is impacted by SBCs more frequently in summer, with stronger daytime and weaker nighttime CL-UHI (Jiang et al. 2019). Analysis of the Shanghai Urban Integrated Meteorological Observation Network (SUIMON, Tan et al. 2015) data identifies there are 65 occurrences of sea breeze fronts (SBFs) in summer (June to September) in the 2011 to 2014 period (Gu et al. 2017). Gu et al. (2017) classify the SBFs into three types (North (N), South (S), and Double (D)) based on where the SBFs appear on land (Fig. 1c, Gu et al. 2017). To investigate the interaction between the UHI and SBC, we focus on the N-type SBF. These usually occur at the mouth of Yangtze River (near the BS site, Fig. 1b) and are associated with thermal conditions making convection likely to be trigged.

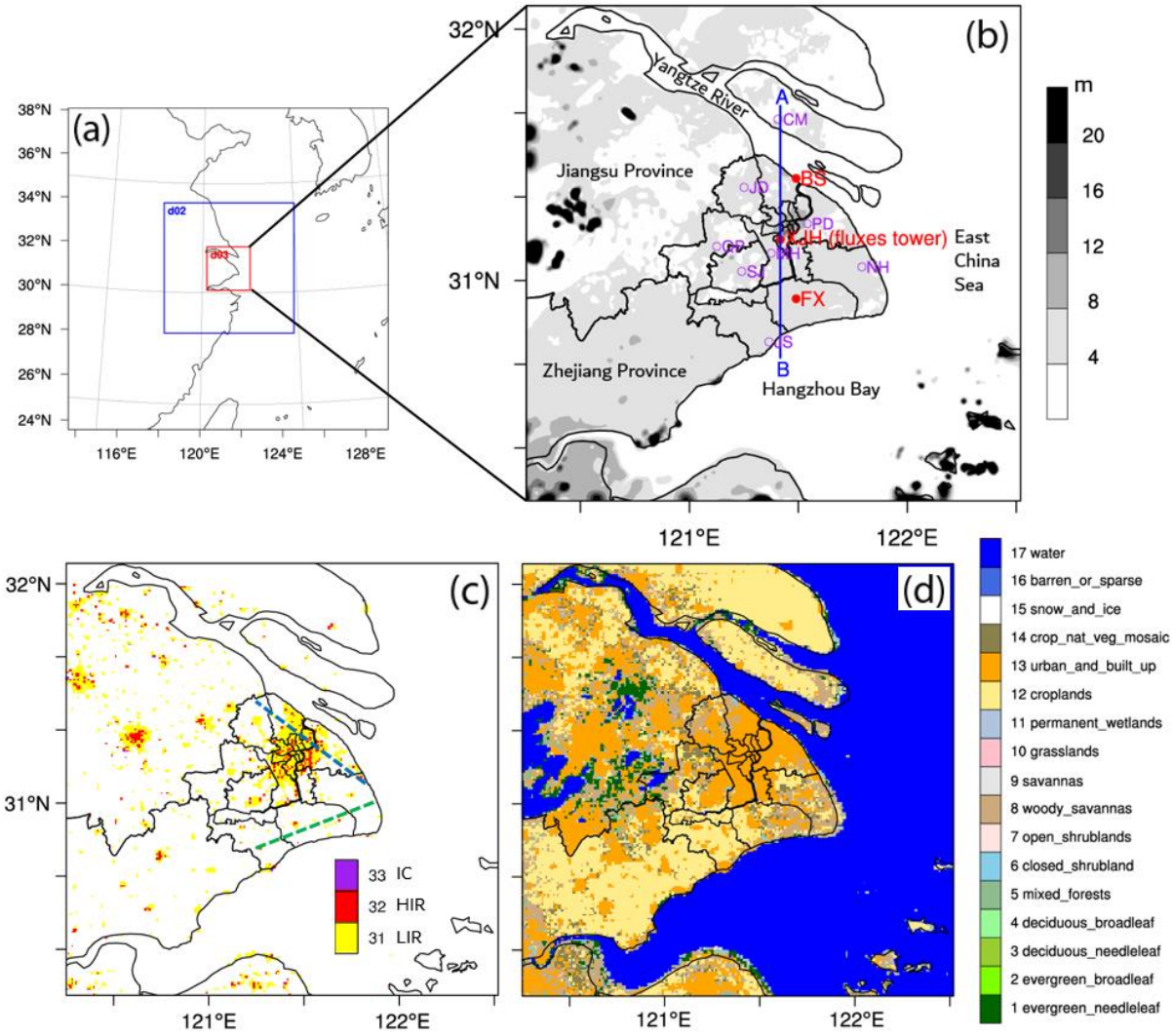


**Figure 1**: Study area: (a) three model domains. For the inner domain: (b) topography, cross-section A-B (blue line at 121.4 °E), and 11 county-level weather stations (dots) with those used for evaluation (filled, e.g., XJH at 31.2°N, 121.4°E); (c) SLUCM urban land-use categories (Li et al. 2015a) and the sea breeze fronts types: North (blue dashed line), South (green dashed line), and Double (blue and green dashed lines), and (d) MODIS MCD12Q1 land use data (500-m resolution).

### *2.2 WRF/SLUCM Model setup*

As noted (section 1), more complex UCMs may not perform better, and the correct prescription of the surface properties is more important than the complexity of the UCM itself (e.g., Grimmond et al. 2011; Lee et al. 2011; Salamanca et al. 2011). From the four most accessible urban land-surface parameterization options within WRF (Chen et al. 2011a), we select the medium complexity - Single Layer Urban Canopy Model (SLUCM, Kusaka et al. 2001; Kusaka and Kimura 2004). For the UHI simulation, the non-built land surfaces are also important. Here we use the Noah land surface model (Chen and Dudhia, 2001).

WRF version 3.8 (released 8 April 2016) coupled SLUCM is used with two-way nesting of three domains with spatial resolutions increasing from 9 to 3 to 1 km. The domains are centered on 31.10°N, 121.37°E (Fig. 1a). The outer domain (181 × 181 grids) covers East China and the adjoining sea, the middle domain covers the Yangtze River Delta (220 × 220 grids), and the inner domain covers the Shanghai region (220 × 220 grids). To simulate boundary layer processes in detail, the vertical dimension is resolved by 48 full sigma levels from surface to 50 hPa, with 39 levels below 2 km. The physical schemes selected (Table 1) are informed by the choices made for many cities when simulating urban atmospheric processes (Loridan et al. 2013, their Appendix 1). The meteorological initial and boundary conditions are interpolated from NCEP (National Center for Environmental Prediction) 0.25° spatial and 6-h temporal resolution global final reanalysis dataset (RDA 2017). Lake and sea surface temperatures are updated daily using NCEP archives (NOAA 2017).

The case study period, 11$^{th}$ to 13$^{th}$ August 2016 during a heat wave, has both a cloudy (12$^{th}$) and a clear (13$^{th}$) day. The simulation is initiated at 0800 LST on 11 August 2016 and ran for 60 hours, with the first 12-h spin up discarded from analysis. All simulation results presented and analyzed are for the inner domain. All times referred are LST.

The land cover data are MODIS (Moderate Resolution Imaging Spectroradiometer) data. In the two outer domains (Fig.1a), 30" spatial resolution 2013 data are downloaded (WRF 2021 V3 Geographical Static Data Downloads Page. For the inner domain, modified 500-m resolution 2010 land cover data (MCD12Q1 - MODIS 2017) are used (Liu et al. 2018). These use the International Geosphere-Biosphere Program (IGBP) land-cover classification (Cohen et al. 2006, Fig. 1d).

We use the SLUCM with three urban categories (Fig. 1c): low-intensity residential (LIR), high-intensity residential (HIR), and industrial/commercial (IC). In these areas, the height and plan area fraction of buildings are assigned values from Shanghai

Surveying and Mapping Institute data (Li et al. 2015a). Given the ability to model the physical processes in the urban environment depends on adequate representation of surface properties and the energy balance (Grimmond et al. 2011; Best and Grimmond 2015), we classify the downtown area with many tall buildings (Tan et al. 2015) as the HIR and derive local parameter values. For the other land uses, we use the v-3.8 parameter values downloaded (Chen et al. 2011a).

The urban surface energy balance is written (Oke 1978):

$$Q^* + Q_F = Q_H + Q_E + \Delta Q_S, \quad (1)$$

where Q* is net all-wave radiation consisting of incoming (↓), outgoing (↑) and net (*) shortwave ($K$) and longwave ($L$) fluxes (Oke 1978):

$$Q^* = [K_\downarrow - K_\uparrow] + [L_\downarrow - L_\uparrow] = K^* + L^*, \quad (2)$$

The terms in Eq. (1) are the anthropogenic heat ($Q_F$), turbulent sensible heat ($Q_H$), turbulent latent heat ($Q_E$), and net storage heat ($\Delta Q_S$) fluxes. Here, the latter flux when 'observed' is estimated by residual in Eq. (1) following others (e.g., Roth and Oke 1994; Roberts et al. 2006).

$Q_F$ can be large in urban areas (e.g., Block et al. 2004; Narumi et al. 2009; Allen et al. 2011; Giovannini et al. 2014). It is often closely related to energy consumption from buildings and traffic (Sailor 2011). Here, we use the Large-Scale Urban Consumption of Energy Model (LUCY) to estimate $Q_F$ (Allen et al. 2011; Lindberg et al. 2013; Gabey et al. 2018) from buildings, traffic, and human metabolism. The building emission includes heat release from air conditioning systems, lighting and other activities. Here $Q_F$ is not split between sensible and latent heat components. Evaporative cooling from air conditioning systems can reduce sensible anthropogenic heat (80-90%) at the expense of latent anthropogenic heat in commercial areas of New York City (Gutiérrez et al. 2015). The traffic data are based on International Road Federation (IFR) World Road Statistics in 2005, with the average traffic speed set to 48 km $h^{-1}$ (Su et al. 2014). The population data are from the 2000 Global Rural Urban Mapping Project (GRUMP). The average daily air temperature data used are from XJH site (August 2016). The calculated daily mean $Q_F$ (84 W $m^{-2}$) and diurnal $Q_F$ cycle (Fig. 2) are used in SLUCM. The LUCY diurnal $Q_F$ cycle is consistent with Shanghai's workday (0900-1700), with 1000-1700 being the peak which is similar to that documented by Li et al. (2015a) for Shanghai, unlike the WRF diurnal $Q_F$ cycle with two peaks at 0800 and 1700.

To determine the HIR parameters, we undertake an offline one at a time (Pitman 1994) sensitivity analysis of SLUCM using version 3.4.1 (released August 2012) using SEB flux measurements observed at XJH (Ao et al. 2016a, b) for a year (December 2012 - November 2013). Each parameter (Table 2) is varied between literature-based minima and maxima (Chen and Dudhia 2001; Loridan et al. 2010) using 100 equal classes. With permutation and combination methods (Zhao et al. 2014a), optimized albedo, thermal conductivity, emissivity and heat capacity values (Table 2) for three facets (roof, road and wall) are determined to minimize the root mean square error (RMSE) of modeled outgoing shortwave radiation flux.

The optimized parameters improve model performance (cf. SLUCM version 3.4.1 downloaded values) for outgoing shortwave radiation with RMSE of 1.5-7.4 W $m^{-2}$ for different seasons, net all wave radiation (7-14 W $m^{-2}$), and the sensible heat flux (2-7 W $m^{-2}$). The optimized albedo, emissivity, and heat capacity for roof, wall, and road in Shanghai (Table 2) are similar, or a bit larger, than those derived using the same optimized method for Nanjing (32.03°N, 118.79°E; Zhao et al. 2014a). The fraction of impervious area (buildings + road, Table 2) or urban built, mean building height and roof width are calculated based on the GIS (Geographic Information System) information for XJH site (Ao et al. 2016a, 2018).

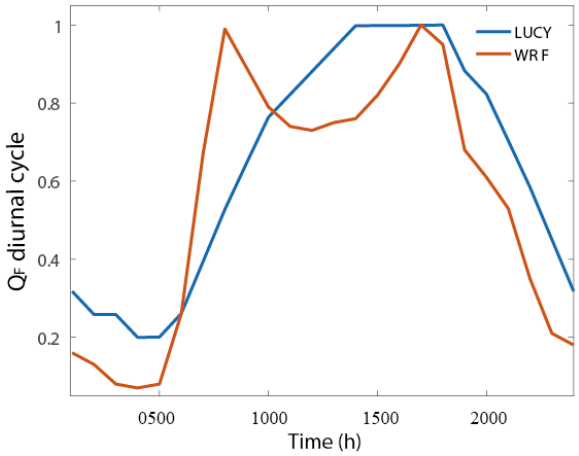


**Figure 2:** Normalized maximum anthropogenic heat flux diurnal cycle on all days. LUCY: Large-Scale Urban Consumption of Energy Model.

**Table 1:** Physical scheme options used in WRF deployment in this study.

| Physics | Option |
|---|---|
| Land surface (non-urban) | Noah LSM (Chen and Dudhia 2001) |
| Urban physics | Single-layer UCM (Kusaka et al. 2001) |
| Microphysics | WSM 6-class (Hong and Lim 2006) |
| Cumulus parameterization | Not used |
| Long-wave radiation | RRTMG (Mlawer et al. 1997) |
| Short-wave radiation | RRTMG (Mlawer et al. 1997) |
| Surface layer | Monin–Obukhov (1954) |
| Boundary layer | Mellor–Yamada–Janjić (MYJ) (Janjić 1994) |

**Table 2:** Parameters values used for the HIR class in Shanghai.

| Parameter (units) | roof | wall | road | Source |
|---|---|---|---|---|
| Fraction of urban built (-) | 0.62 | | 0.23 | Ao et al. (2018) |
| Building height (m) | | 36 | | Ao et al. (2016a) |
| Roof width (m) | 25 | | | Ao et al. (2016a) |
| Heat capacity (MJ $m^{-3}$ $K^{-1}$) | 1.4 | 1.0 | 1.4 | This paper |
| Thermal conductivity (J $m^{-1}$ $s^{-1}$) | 0.6 | 0.67 | 0.4 | This paper |
| Surface albedo (-) | 0.16 | 0.14 | 0.13 | This paper |
| Surface emissivity (-) | 0.85 | 0.95 | 0.95 | This paper |

### *2.3 Meteorological Observations*

In this study, four types of observations are used:

1) *Urban fluxes:* Instruments wired to a Campbell Scientific CR3000 data logger are mounted 80 m above ground level (AGL) at XJH site located in a central business district (CBD), which is modelled here as HIR (Ao et al. 2016a, b). The radiation fluxes are measured with a Kipp and Zonen CNR4 net radiometer, and turbulent fluxes measured with a Campbell Scientific IRGASON open-path infrared absorption gas analyzer integrated with a three-dimensional sonic anemometer. For any terrain, eddy covariance (EC) measurements need to be made at least twice the height of the roughness elements to ensure that the equipment is within the inertial sub-layer (ISL) or constant flux layer (CFL; Grimmond and Ward 2021). So when flux measurements from ISL are defined as local-scale, while that from roughness sub-layer (RSL) are defined as micro-scale (Ao et al. 2016a; Grimmond and Ward 2021). As Ao et al. (2016a) indicates, EC sensor (i.e., the IRGASON) at XJH is not high enough to give local-scale measurements in all wind directions (i.e., some are micro-scale fluxes), the $Q_H$ and $Q_E$ are thus stratified by wind direction. Fluxes are analyzed using 30-min means.

(2) *11 county-level weather stations (Fig. 1b):* Shanghai Climate Center provides both automatic and manual quality-controlled (Sun and Hu 2009) hourly 2 m AGL air ($T_2$) and dew point ($T_{d,2}$) temperature, 10 m AGL wind speed ($WS_{10}$) and direction ($WD_{10}$), plus 80 m AGL wind speed ($WS_{80}$) and direction ($WD_{80}$) at XJH.

(3) *Approximately 900 Automatic weather stations (AWS) quality controlled by the Shanghai, Jiangsu and Zhejiang Meteorological Services (Fig. 6d-f):* Jiangsu Radio Scientific Institute Co. Ltd DZZ4 AWS sensors measure $T_2$, $WS_{10}$, and $WD_{10}$ (SUIMON, Tan et al. 2015). Data analyzed are hourly means.

(4) *Upper-air soundings:* are released every 6-h at BS site (Fig .1b) can provide 10 m vertical resolution profiles of temperature, humidity, wind speed, and direction below 2 km for 1400 on 13 August 2016.

### *2.4 Model Verification*

To evaluate the model performance using observations energy fluxes and other meteorological variables (Table 4), two statistical metrics are used: mean bias error (MBE) and mean absolute error (MAE). The statistics are performed for different time periods including day ($K_\downarrow > 0$ W $m^{-2}$) and night (remainder of the hours).

The model output evaluated is the median values of nine (3 × 3) grids around each site. For the 80 m observations level (wind at XJH), the model output from first (lowest: 52.6 m AGL) and second (117.6 m AGL) levels are interpolated for analysis. In WRF, $T_2$ is diagnosed from lowest model layer height and surface (Shin and Hong 2011) calculated from the sensible heat flux (Li and Bou-Zeid 2014):

$$T_2 = T_s - \frac{Q_H}{\rho C_{h2} U_2} \ . \qquad (3)$$

This uses the grid (i.e., land cover fraction weighted tiles values) of surface temperature ($T_S$), $Q_H$ and air density ($\rho$), wind speed at 2 m ($U_2$), and a heat transfer coefficient ($C_{h2}$) assuming Monin - Obukhov Similarity Theory (MOST; Monin and Obukhov 1954) holds. $U_2$ is obtained from $U_{10}$. $U_{10}$ also assumes MOST (Strassberg et al. 2008):

$$u_{10} = \frac{u_*}{k}\left[\ln\left(\frac{z_{10}}{z_0}\right) - \Psi_M\left(\frac{z_{10}}{L_{mo}}\right)\right] , \qquad (4)$$

where $u^*$ is friction velocity, $k$ the von Kárman constant, $z_0$ is roughness length for momentum, and $\Psi_M$ is the stability function which is a function of Obukhov length $L_{mo}$ (Garratt 1994). This includes several poor but widely used assumptions including (Loridan et al. 2013; Kent et al. 2017; Theeuwes et al. 2019): MOST and the logarithmic law only apply in the ISL (or CFL). So the RSL, urban canopy layer, and zero plane displacement are not accounted for despite the tallness of the roughness elements.

The observed CL-UHI intensity ($T_2$) is based on the XJH (urban) and FX (exurban site, in southern area, Fig. 1b). The land cover characteristics within 1-km radius of these sites are given in Table 3. The wind and temperature distribution across the inner domain are analyzed at various key times (0800, 1400, 2000 for air temperature; 1200, 1300, 1400, 1500 for wind), which can capture the variation of UHI and SBFs evolution on 13 August 2016 using both MBE and MAE spatially within 10×10 raster (with 22 × 22 = 484 grid cells per raster). SBF evolution (A-B cross section, Fig. 1b) is derived from $v$ (S to N) zonal wind component, $w$ vertical velocity, and $q$ water vapor mixing ratio.

**Table 3:** Land cover characteristics within 1-km radius and local climate zone (LCZ) classes (Stewart and Oke 2012) of measurement sites used for model evaluation.

| Site | Type | Location | Land Cover (%) | | | | Source | Local Climate Zone |
|---|---|---|---|---|---|---|---|---|
| | | | Building | Pavement | Vegetation | Open water | | |
| XJH | Urban | city center | 25 | 58 | 17 | 0 | Ao et al., 2016a | LCZ 1 |
| BS | Suburban | northern coast | 17 | 28 | 52 | 3 | Liu et al., 2018 | LCZ 5 |
| FX | exurban | southern inland | 14 | 20 | 65 | 1 | Liu et al., 2018 | LCZ 6 |

**Table 4:** Notation and number of data points (N) available for analysis under different conditions in the period from 20:00 11th to 20:00 13th August 2016 with a total N=97.Table 6 and section 3 defined micro and local scale for eddy covariance (EC) fluxes. Day: $K_{\downarrow} > 0$ W m$^{-2}$

| Flux density (30 min) | | | | | | | EC scale | |
|---|---|---|---|---|---|---|---|---|
| | | | Day | Night | Cloudy | Clear | Local | Micro |
| Radiation | $K_{\downarrow}$ | Incoming shortwave | 55 | 42 | 49 | 48 | | |
| | $K_{\uparrow}$ | Outgoing shortwave | | | | | | |
| | $L_{\downarrow}$ | Incoming longwave | | | | | | |
| | $L_{\uparrow}$ | Outgoing longwave | | | | | | |
| | $Q^*$ | Net all-wave radiation | | | | | | |
| Turbulent | $Q_H$ | Sensible heat | | | | | 45* | 52* |
| | $Q_E$ | Latent heat | | | | | | |
| | $\Delta Q_S$ | Net storage heat | | | | | | |
| Near-surface meteorological variables (60 min) | $T_2$ | 2 m AGL air temperature | N=49 | | | | | |
| | $T_{d,2}$ | 2 m AGL dew point temperature | | | | | | |
| | $WS_{10}$ | 10 m AGL wind speed | | | | | | |
| | $WD_{10}$ | 10 m AGL wind direction | | | | | | |

## 3. Results of WRF/SLUCM Evaluation

WRF/SLUCM is evaluated using a series of observations. First, we consider the energy balance fluxes at the CBD site, XJH. Fig. 3a shows the simulations have the expected diurnal pattern with more deviation from the median (line) on the cloudy than the clear day due to the influence of cloud.

Incoming shortwave radiation, $K_{\downarrow}$, is overpredicted (MBE =115 W m$^{-2}$, Table 5) with better performance on the clear (MBE= 61 W m$^{-2}$) than the cloudy (163 W m$^{-2}$) day (Fig. 3a). This result is consistent with previous studies using the Rapid Radiative Transfer Model for Global Climate Models (RRTMG) radiation scheme (Iacono et al. 2008), which is found positive biases during clear skies (e.g., Ruiz-Arias et al. 2016). When cloud is present, there is added uncertainty from predicting cloud location (e.g., Feudo et al. 2015). As expected, given the over-prediction of $K_{\downarrow}$ the simulated $K_{\uparrow}$ also has a positive MBE (30 W m$^{-2}$, Fig. 3b, Table 5), which is larger for the cloudy (35 W m$^{-2}$) than the clear day (25 W m$^{-2}$).

However, the modeled $L_{\downarrow}$ have a negative MBE (-22 W m$^{-2}$), with better performance on the cloudy (-17 W m$^{-2}$) than the clear (-27 W m$^{-2}$) day (Fig. 3c). The underestimation of $L_{\downarrow}$ maybe attributed to not taking the aerosol effects into consideration. $L_{\uparrow}$ depends on the total incoming radiation energy ($K_{\downarrow}$+ $L_{\downarrow}$), conduction and convection heat exchanges, and hence the nature of the urban surface facets (Ao et al. 2016a). The offset between the overestimated $K_{\downarrow}$ and underestimated $L_{\downarrow}$, helps $L_{\uparrow}$ match the observed values well especially during the daytime. The overall $L_{\uparrow}$ MBE is small (-1 W m$^{-2}$) on both days (Fig. 3d, Table 5).

The modelled net all-wave radiation, $Q^*$, has a positive MBE (54 W m$^{-2}$) during the day and a smaller negative MBE (-8 W m$^{-2}$) at night. Overall, there is a positive MBE (27 W m$^{-2}$, Fig. 3e, Table 5) for $Q^*$. The main cause of the daytime bias is the positive bias in modelled $K_{\downarrow}$.

Given the complexity of the urban site, the eddy covariance (EC) sensor is not always within the inertial sublayer (ISL) and therefore satisfying the requirements to be a local scale measurement (Grimmond et al. 2005, Ao et al. 2016, Grimmond and Ward 2021). When the EC sensor is within the roughness sub-layer (RSL), this is greater observational uncertainty of the turbulent fluxes and the measurements do not represent the local scale, rather they are micro-scale. The modelled turbulent heat fluxes are assumed to be local scale fluxes.

The modelled sensible heat fluxes ($Q_H$) are systematically underpredicted during the day (MBE = -128 W m$^{-2}$) and night (MBE = -98 W m$^{-2}$, Fig. 3f). During day and night, the local-scale $Q_H$ metrics (MAE, MBE) are better than for the micro-scale fluxes (Table 6). Both the simulated and measured $Q_E$ are very low in this area as there only 17 % of the plan area is vegetation (Fig. 3g, Table 3). The underpredicted $Q_E$ (MBE = -22 W m$^{-2}$) may be related to the low initial conditions in the model for soil moisture, or more likely, irrigation being unaccounted for in WRF/SLUCM (Ao et al. 2018).

To evaluate the modeled net storage heat flux, $\Delta Q_S$ observations are also restricted to times with local scale EC fluxes. Modeled $\Delta Q_S$ is overestimated during the day (MBE = 20 W m$^{-2}$) and underestimated at night (MBE=-109 W m$^{-2}$, Table 6), with better performance on the clear day (Fig. 3h). As with all the fluxes the over-prediction of $K_{\downarrow}$ should cause a subsequent overprediction of the other fluxes. The underprediction of $Q_H$ and $Q_E$ is also explained by the underestimated $Q_F$ compared to Ao et al. 2018 (mean value: 156.3 W m$^{-2}$ at XJH from June to August) and Li et al. 2015a (2010 annual mean: 117.7 W m$^{-2}$).

Additionally, air temperature ($T_2$), dew point temperature ($T_{d,2}$), 10 m wind ($WS_{10}$ and $WD_{10}$) observations in the urban canopy layer at three sites (Fig.4, Table 7) are used to evaluate the model. The model performance for $T_2$ is little poorer at the north suburban BS site (MAE= 1.2°C) than at the exurban FX site (MAE=0.9°C) because the modeled sea breeze occurred earlier than observed near BS site and with cooler temperature.

The model performance for $T_{d,2}$ at urban XJH (MAE=1.1°C) is better than that at suburban BS and exurban FX. For almost all variables, the model performs best at urban XJH. The exception is for wind direction. This suggests the HIR class parameter optimization (Section 2.2, Table 2) is beneficial. The 10 m AGL wind speed MAE is above 1.5 m s$^{-1}$ at the suburban and exurban sites. The within canopy (10 m AGL) winds assume MOST, hence this may contribute to the poor performance in predicting wind speeds (Theeuwes et al. 2019). However, the prevailing synoptic easterlies (10 m at BS and FX sites and 80 m at XJH site) are captured well by WRF/SLUCM (Fig. 4j-l) with MBE of $WD < 25°$, while MBE of $WS_{10}$ at BS site is about 3.2 m s$^{-1}$, it is also due to the modelled sea breeze occurred earlier near BS site and enhance sea breeze.

In general, WRF/SLUCM captures the sea breeze well on the clear day (13 August). However, the simulated sea breeze is an easterly but the observed sea breeze is a northeasterly on 13 August. At BS site, the modeled change in wind direction is accompanied by an increase $WS_{10}$ (e.g., 1200, Fig. 4h, k). The observed wind direction obviously shifts at northern coastal BS site (from south-east to north-east) on both days (Fig. 4h). It is accompanied by a small fluctuation in air temperature (Fig. 4a). The sea breeze is well developed by noon (i.e., solar radiation peak), continues until ~1600, and disappears at sunset when the solar radiation decreases rapidly when the modeled air temperature is very close to the model (assigned) sea surface temperature. Given the WRF/SLUCM model with local parameters for the HIR area can reproduce the surface air temperature, humidity, wind, and radiation/fluxes reasonably well, we use it to examine the diurnal variation of the UHI, temporal and spatial evolution of SBC, and their interaction over Shanghai.

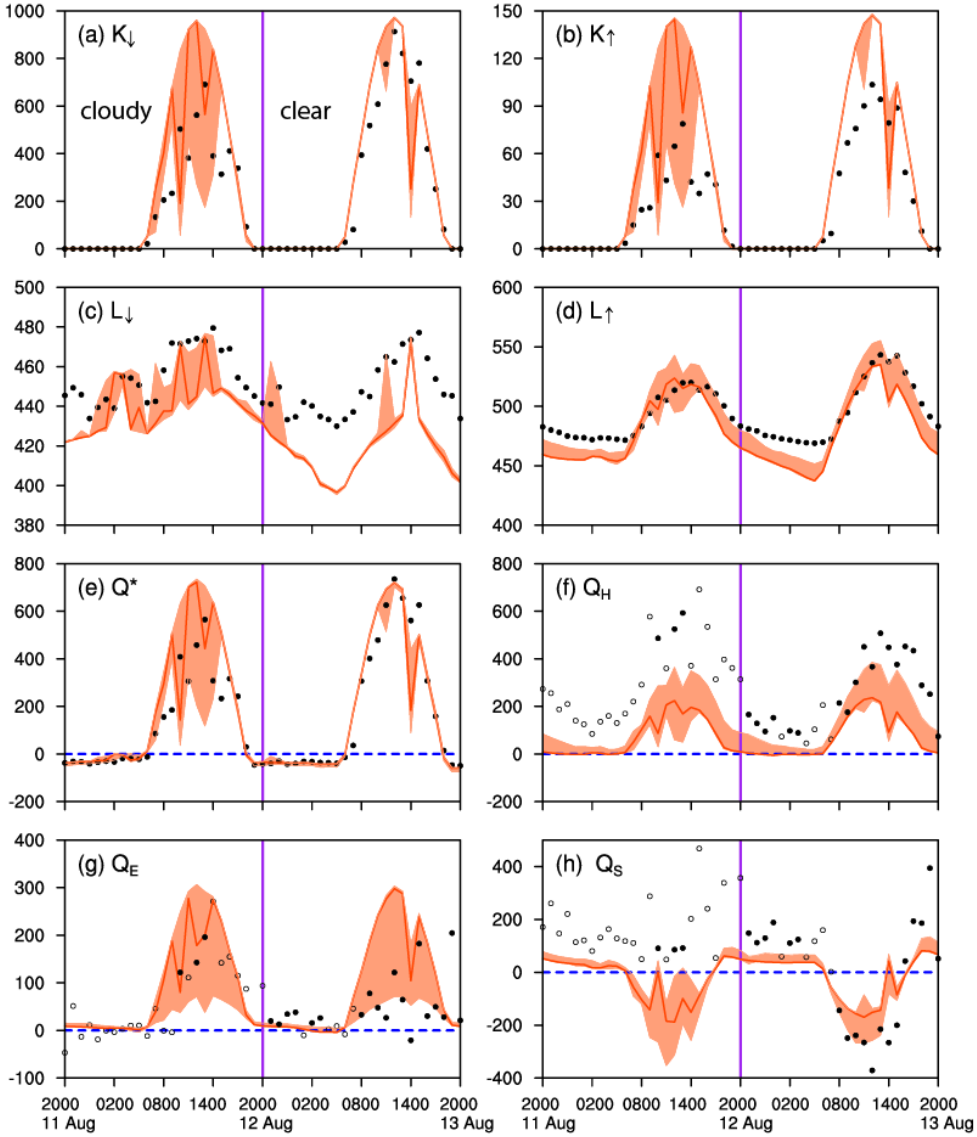


**Figure 3:** Observed (black dots: local-scale; black circle: micro-scale) and modelled (3 × 3 grid) maximum and minimum range (shaded), median (orange line) radiation and heat fluxes (unit: W m$^{-2}$) at XJH during 11 - 13 August 2016 (a) $K_{\downarrow}$, (b) $K_{\uparrow}$, (c) $L_{\downarrow}$, (d) $L_{\uparrow}$, (e) $Q^*$, (f) $Q_H$, (g) $Q_E$, (h) $\Delta Q_S$. Purple line split cloudy and clear days (both having 24 h periods). Table 4 defines the notation.

**Table 5:** Mean radiative fluxes modelled (surface) and observed at XJH by time of day, with performance metrics (Section 2.4). Table 4 gives the notation and number of values analyzed by class. See Table 6 for other SEB fluxes.

| Fluxes (W m$^{-2}$) | Model | | | Observation | | | MBE | | | MAE | | |
|---|---|---|---|---|---|---|---|---|---|---|---|---|
| | Day | Night | All | Day | Night | All | Day | Night | All | Day | Night | All |
| $K_{\downarrow}$ | 498 | - | - | 383 | - | - | 115 | - | - | 160 | - | - |
| $K_{\uparrow}$ | 75 | - | - | 45 | - | - | 30 | - | - | 33 | - | - |
| $L_{\downarrow}$ | 434 | 424 | 430 | 459 | 442 | 452 | -25 | -18 | -22 | 25 | 20 | 23 |
| $L_{\uparrow}$ | 512 | 466 | 492 | 506 | 476 | 493 | 6 | -10 | -1 | 11 | 10 | 11 |
| $Q^*$ | 345 | -42 | 177 | 291 | -34 | 150 | 54 | -8 | 27 | 107 | 11 | 66 |

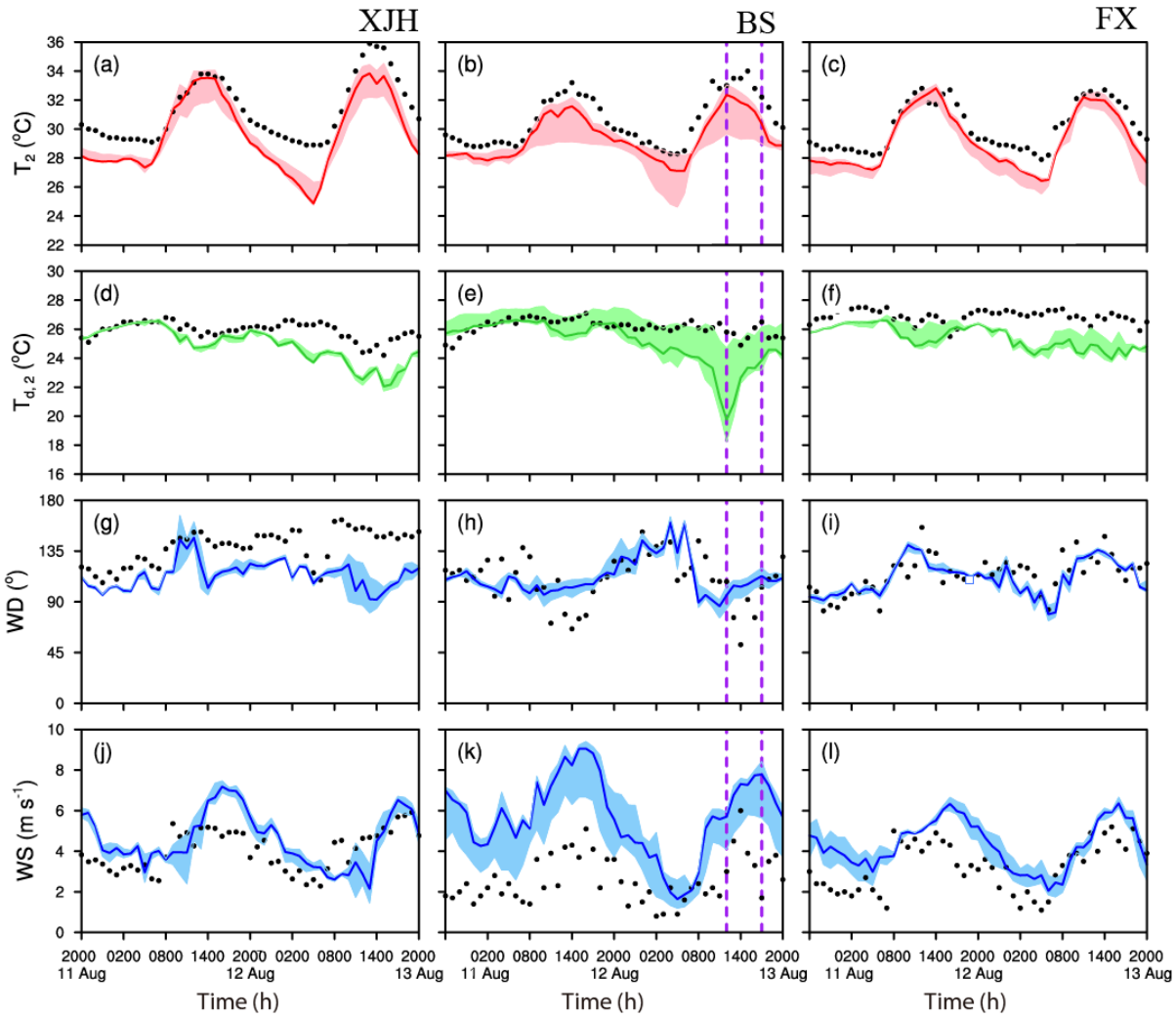


**Figure 4:** Observed (black dots) and modelled (3 × 3 grid) maximum and minimum range (shaded), median (line) at XJH, BS, FX sites (columns, sites see Fig. 1) for (**a-c**) 2-m air temperature (°C),(**d-f**) 2-m dew point temperature (°C), 80-m tower wind (**g**) direction (°) and (**j**) speed (m $s^{-1}$), (**h-i**)10-m wind direction (°) and (**k-l**) speed (m $s^{-1}$). Duration of the sea breeze at BS station (purple dashed lines).

**Table 6**: As Table 5, stratified by scale based on wind direction which is associated with urban morphology, and therefore flux uncertainty associated with the eddy covariance (EC) sensor being within the inertial sublayer (ISL) or roughness sublayer (RSL). Ideally the sensor is within the ISL, to give local-scale (L) measurement (N=45 hours). If the EC sensor is within the RSL there is larger observational uncertainty for evaluating the local-scale modelled fluxes as the observations are defined as being micro-scale (M). (N= 52 hours).

| Flux ($W m^{-2}$) | Model when observations are defined at M or L | | | | | | Observation | | | | | |
|---|---|---|---|---|---|---|---|---|---|---|---|---|
| | Day | | Nocturnal | | All | | Day | | Nocturnal | | All | |
| Scale | M | L | M | L | M | L | M | L | M | L | M | L |
| $Q_H$ | 167 | 277 | 43 | 60 | 101 | 209 | 320 | 386 | 160 | 120 | 234 | 303 |
| $Q_E$ | 33 | 52 | 11 | 13 | 21 | 40 | 63 | 98 | 2 | 32 | 29 | 77 |
| $\Delta Q_S$ | -50 | -70 | 34 | 48 | -7 | -27 | 173 | -90 | 152 | 157 | 162 | 0 |
| | MBE | | | | | | MAE | | | | | |
| $Q_H$ | -153 | -109 | -117 | -61 | -134 | -94 | 156 | 139 | 117 | 66 | 135 | 116 |
| $Q_E$ | -30 | -46 | 9 | -19 | -9 | -37 | 43 | 60 | 20 | 31 | 31 | 51 |
| $\Delta Q_S$ | -210 | 20 | -119 | -109 | -162 | -27 | 219 | 142 | 119 | 113 | 167 | 131 |

**Table 7:** Performance metrics with mean values observed (O) and modeled (M) at three stations (Fig. 1b) for four meteorological variables.

| Variables | Station | Height (AGL) | $Mean_M$ | $Mean_O$ | MBE | MAE |
|---|---|---|---|---|---|---|
| $T_2$ (°C) | XJH | 2 m | 30.2 | 31.2 | -1.0 | 1.1 |
| | BS | 2 m | 29.4 | 30.6 | -1.2 | 1.2 |
| | FX | 2 m | 29.3 | 30.2 | -0.9 | 0.9 |
| $T_{d,2}$ (°C) | XJH | 2 m | 24.8 | 25.9 | -1.1 | 1.1 |
| | BS | 2 m | 25.0 | 26.1 | -1.1 | 1.3 |
| | FX | 2 m | 25.4 | 26.9 | -1.5 | 1.5 |
| $WS$ ($m s^{-1}$) | XJH | 80 m | 4.6 | 4.0 | 0.6 | 1.1 |
| | BS | 10 m | 5.8 | 2.6 | 3.2 | 3.2 |
| | FX | 10 m | 4.6 | 3.2 | 1.4 | 1.5 |
| $WD$ (°) | XJH | 80 m | 114 | 139 | -25 | 25 |
| | BS | 10 m | 112 | 111 | 1 | 17 |
| | FX | 10 m | 111 | 114 | -3 | 11 |

## 4. Urban heat island (UHI) and sea breeze circulation (SBC) results

### *4.1 Canopy-layer UHI (CL-UHI)*

As expected, of the two study days the intensity of CL-UHI is weaker on cloudy (12th August) day. On the clear 13th August, the observed highest intensity occurs early afternoon ($CL\text{-}UHI_{obs}$ = 3.5°C at 1300) and shortly after sunrise there is no CL-UHI ($CL\text{-}UHI_{obs}$ = -1.0 °C at 0700, Fig. 5). However, the modeled median CL-UHI on the same day varies between 2.7 °C (1500 LST) and -0.7°C (0500 LST), with a cool island continuing to 0900 LST.

In Shanghai, the summer CL-UHI is largest during the day mainly because of the sea breeze. Southeasterly winds from the sea cools exurban FX (Fig. 1b and 6b, e), enlarge the temperature difference between the urban center and the southeastern suburbs. WRF/SLUCM simulates the CL-UHI spatial pattern well. At 0800 LST, the CL-UHI is weak, when surface heating is beginning in both areas, so near surface air temperatures are similar (Fig. 6a, d). At 1400 LST, the CL-UHI is strongest in the mid-north given the prevailing southeast wind and sea breeze causing the CL-UHI center to be advected to northwest (Fig. 6b, e). In the evening (2000 LST, Fig. 6c, f), the CL-UHI weakens but is maintained by large storage heat release slowing the radiative cooling of the city and maintaining the $Q_H$ through the night. The spatial pattern of air temperature MBE (Fig. 7) is mostly negative (-1 to -2°C) and the range of MAE is 1 - 3°C at the three evaluation times. The model performs better in south central Shanghai (MBE = 0 to -1°C, MAE = 0 to 2°C), perhaps given the use of locally derived urban parameters.

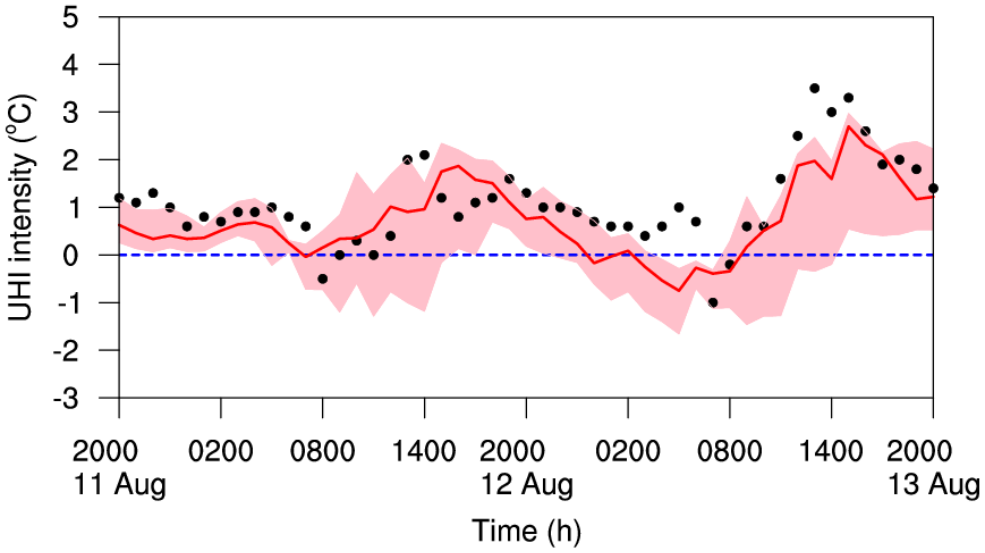


**Figure 5:** As Fig. 3, but canopy layer UHI (2 m AGL) intensity (XJH – FX).

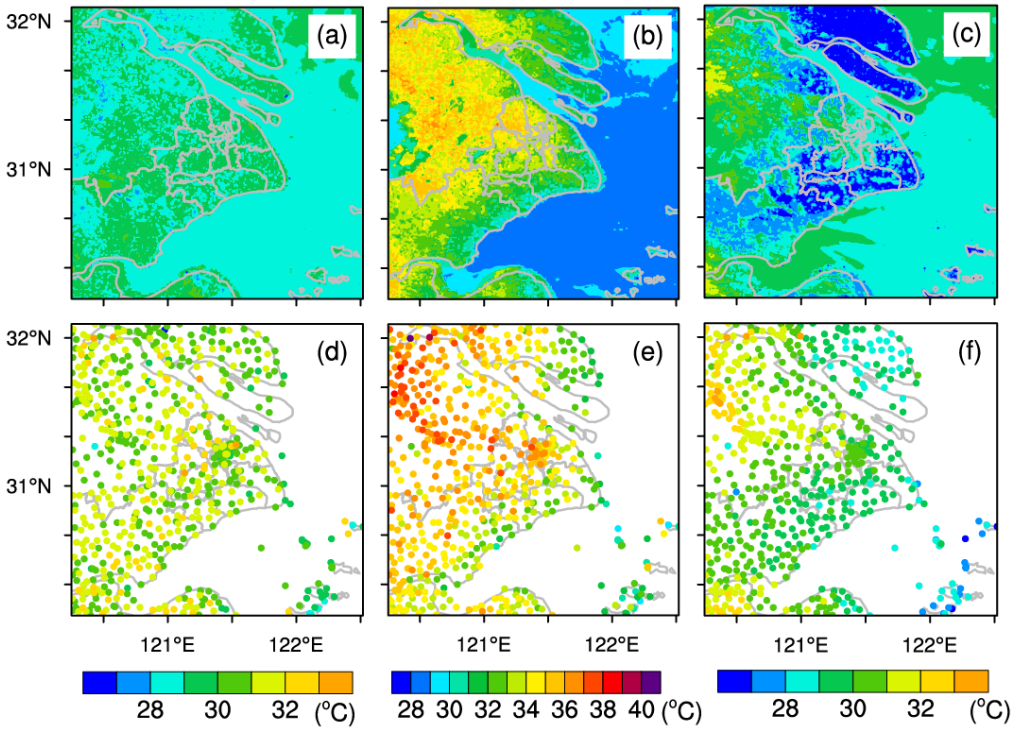


**Figure 6:** Near-surface (2 m AGL) air temperature distribution on 13 August 2016: (**a-c**) simulated and (**d-f**) observed at (**a, d**) 08:00, (**b, e**) 14:00, and (**c, f**) 20:00.

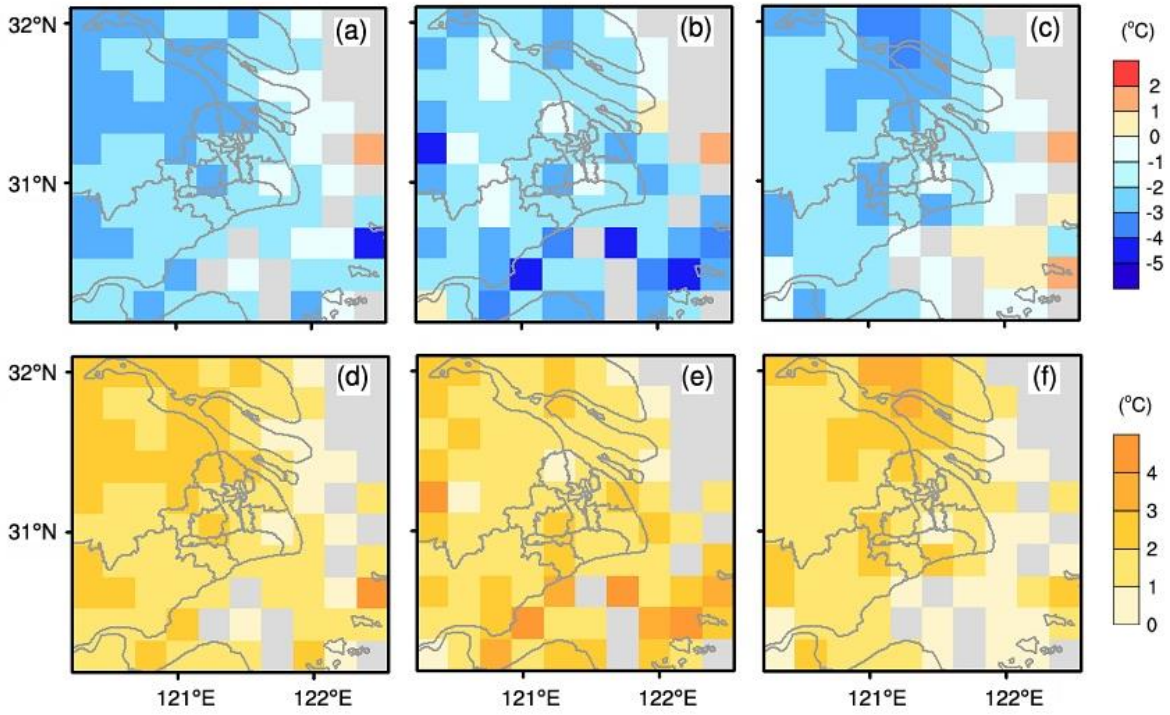


**Figure 7:** Spatial distribution of: (**a-c**) MBE and (**d-f**) MAE (each raster: 22 km × 22 km) of near-surface (2 m AGL) air temperature at (**a, d**) 08:00, (**b, e**) 14:00, and (**c, f**) 20:00 on 13 August 2016.

### *4.2 Sea breeze*

Under these southerly conditions, the SBF comes on land at the mouth of Yangtze River in northern Shanghai, near BS site (i.e., N-type). Simulated (Fig. 8) and observed (Fig. 9) 10 m AGL wind field and divergence show the evolution of the sea breeze from both southeast and northeast towards Shanghai coast from 1200 to 1500 LST. From the wind field, it is clear that the northeast wind begins to blow onshore at ~1200 LST (13 August) under the prevailing southeast background wind (Fig. 8a, Fig. 10a; i.e., indicating the onset of the sea breeze). The interaction between the sea-breeze and background wind generates shear that develops inland reaching the northeastern suburbs of Shanghai (~5 km from the coast). At the same time, the southeast sea breeze at Hangzhou Bay (see Fig. 1b for location) merges with the background surface wind, reinforcing the southeast wind and inland penetration. As the land surface becomes warmer, the sea breeze strengthens both at the Yangtze River estuary and Hangzhou Bay. The SBF, inferred from wind shear and the edge of scattered wind convergence, moves inland nearly 20 km toward to the urban center (Fig. 8a, b; 9a, b). By 1400-1500 LST, the observed inland penetration is retarded (Fig. 9c, d) by the larger urban surface roughness, as observed elsewhere (e.g., NYC, Bornstein and Johnson 1977). However, the simulated SBF penetrates up to ~40 km (Fig. 8c, d) suggesting the prescribed urban surface roughness in WRF/SLUCM is too small. By 1500 LST (Fig. 8d), the modeled SBF is through XJH, the most densely built area with largest roughness. It becomes distorted as it moves inland at different rates. From the Yangtze River estuary the sea breeze becomes easterly. In the afternoon, one consequence of the interaction between urban heating and SBFs is the appearance of low-level convergence over and downwind of the urban area (Fig. 8 shaded). As the low-level humidity is enhanced by transport from the sea, shallow convection develops and forms cumulus clouds. The clouds reduce incoming short-wave radiation, causing a rapid decrease in outgoing short- and long-wave radiation (Fig. 3). Subsequently, both the intensities and areas influenced by the sea breeze and wind shear gradually weaken as temperature differences between the coastal urban land and the sea decreases.

The spatial MBE of wind speed (Fig. 10) suggests the model can be used to simulate the sea breeze, with positive bias (< 2 m $s^{-1}$ at 1200 and 1400 LST; 2 - 4 m $s^{-1}$ at 1300 and 1500 LST) across Shanghai which may attribute to the underestimation of the surface roughness. The MAE range is 1 - 4 m $s^{-1}$ (1 - 2 m $s^{-1}$ at 1200 and 1400 LST; 2 - 4 m $s^{-1}$ at 1300 and 1500 LST). In southeast of Shanghai, there is relatively large bias owing to the windward model domain lateral boundary effects.

The easterly observed below 1000 m in the simulated wind profile at BS site has increasing speeds from 1200 to 1600 LST (Fig. 11b). Lower in the observed profile (< 200 m, Fig. 11c, 1400 LST), there is a northeasterly flow (> 5 m $s^{-1}$) implying the sea breeze has developed at BS by noon. The resulting enhanced horizontal momentum (BS site at 1200 LST) causes vertical shear (east to south, clockwise with height) from 500 to 1500 m. This implies warm advection occurs as the land rapidly heats. Accompanying this, humidity increases and temperature decreases as the sea breeze develops at BS (Fig. 4 b, e). It lasts about 4 hours, ending at ~1600 LST when the wind returns to the background synoptic direction (south-easterly). Urban XJH is affected by the modeled sea breeze after 1400 LST, about 2-h later than it arrived at BS. The easterly wind direction, and increase in wind speed, are clear in both their time and height (Fig. 4g, j, 11a).

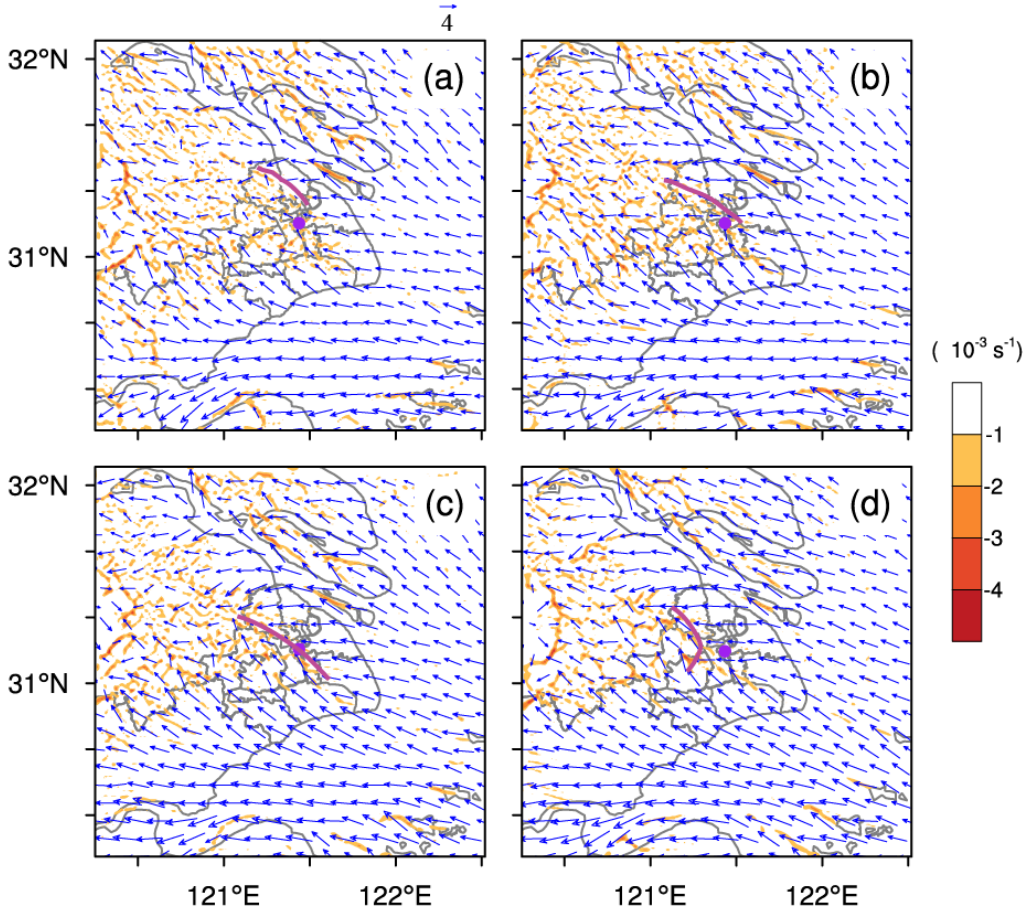


**Figure 8:** Simulated 10 m AGL wind (vectors) and divergence ($10^{-3}$ $s^{-1}$, key) with position of urban center (purple dot) and sea breeze front (purple line) on 13 August 2016 at (a) 12:00, (b) 13:00 , (c) 14:00, and (d) 15:00.

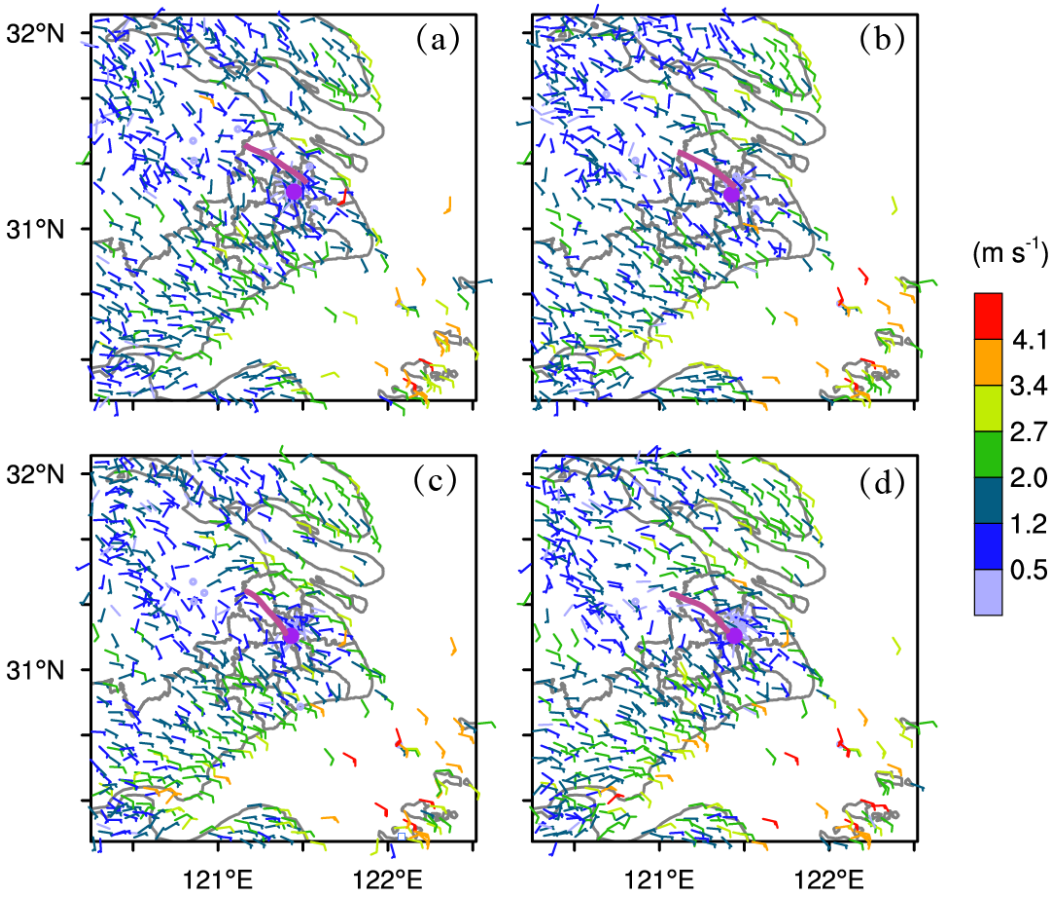


**Figure 9:** As Fig. 8, but observed 10 m AGL wind (barbs) field and the position of sea breeze front (purple line).

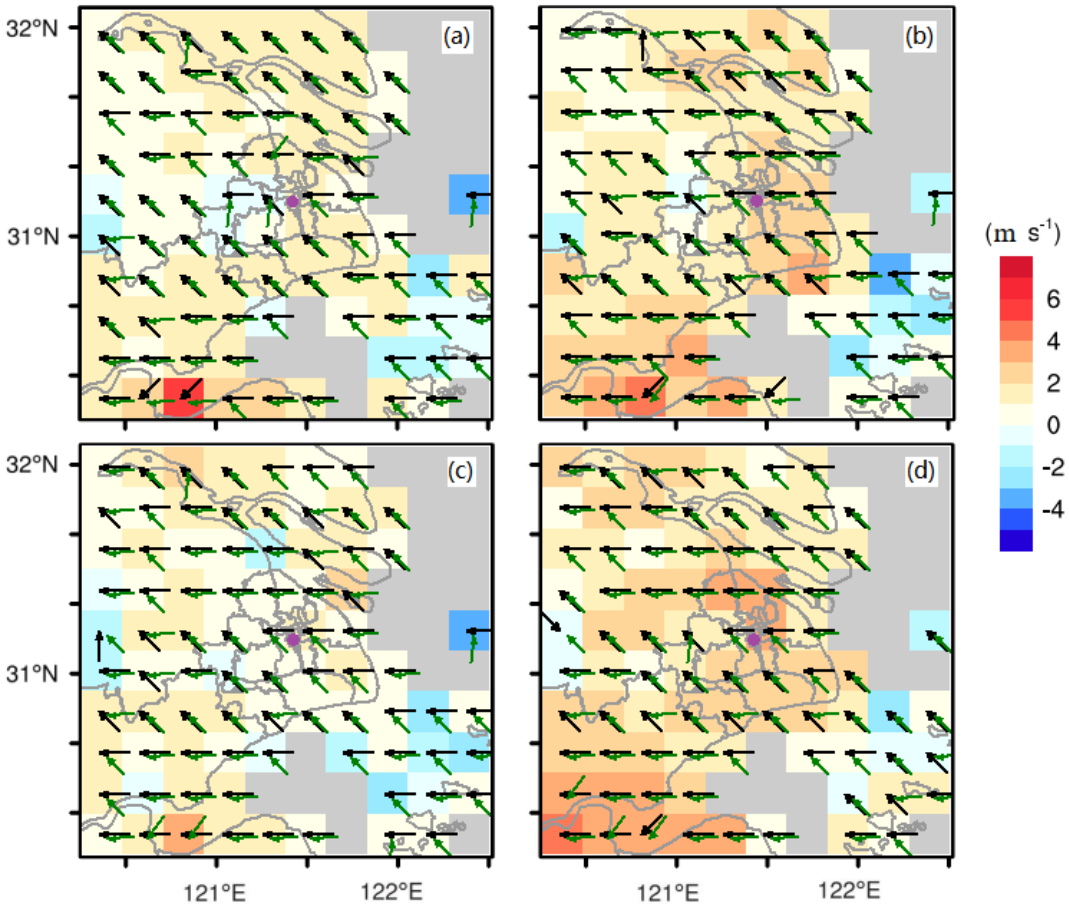


**Figure 10:** As Fig. 7, but MBE distribution of wind speed (color) and dominant wind direction (arrows AWS: black, WRF: green) for times as Fig. 8.

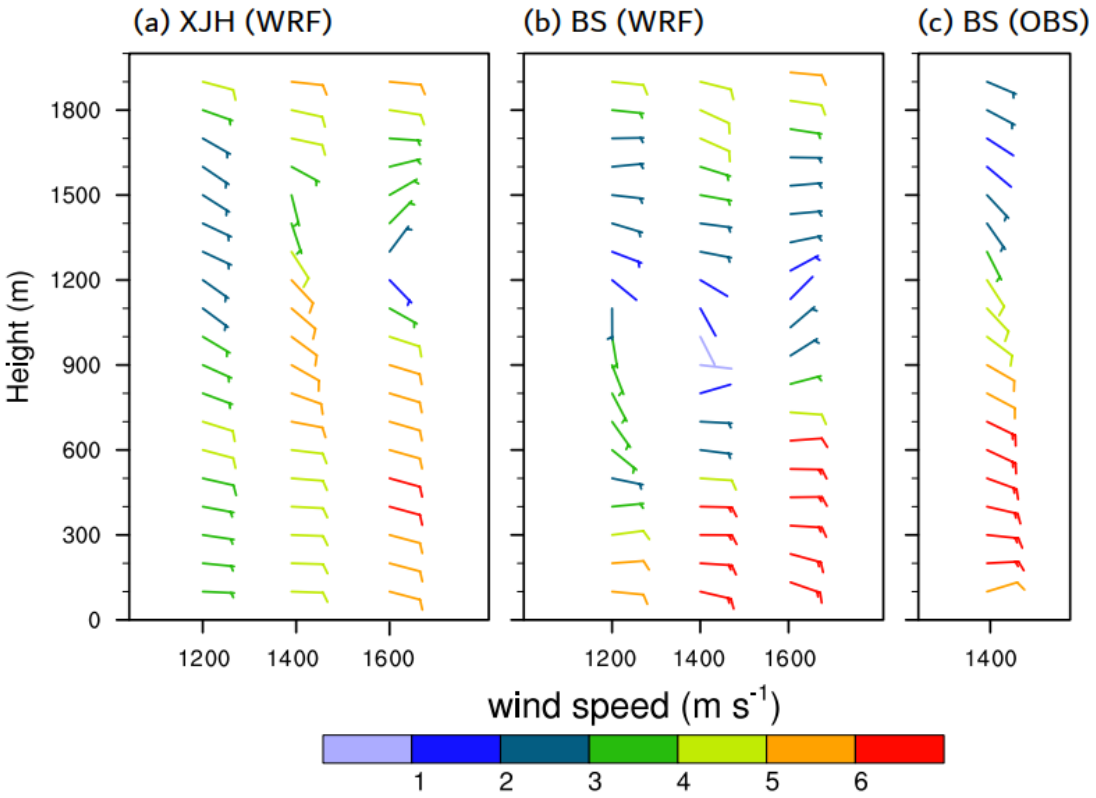


**Figure 11:** Wind profiles at: (**a**) XJH (simulated), (**b**) BS (simulated), and (**c**) BS (observed) on 13 August 2016.

### *4.3 Interaction of UHI and SBC*

To further investigate the effect of urban area on sea breeze development, a cross section between the urban center (XJH), Hangzhou Bay, and the Yangtze River estuary (line AB, 121.43°E, Fig. 1b) is analyzed (Fig. 12, 13). At 0800 LST (Fig.12a, 13a), given the minimal differences in surface heating, a stable atmosphere neither the UHI nor the sea-breeze occur. From 1200 to 1500 LST (Fig. 12b-e, 13b-e), the heat island circulations start to develop especially upwind of the built-up area, while the sea breeze is

retarded from moving further inland given interactions with the heat island circulation.

The urban warms the boundary layer up to 1.5 km. The urban area is ~3.0°C warmer (cf. surrounding countryside). Near 31.1-31.2°N, there are increased vertical velocities (up to ~1.5 m $s^{-1}$) from the surface to 2 km with descending motion near 31.3°N. These form urban-breeze circulations lasting for 3 hours with horizontal span of ~20 km and vertical span of nearly 1.5 km. The evolution of the sea breeze is also modified. At noon, the urban area enhanced land-sea temperature differences accelerate the sea breeze. Given the built-up area is concentrated to the north and center of Shanghai, it causes a larger temperature gradient between the land and sea to the north (cf. south). When the sea breeze reaches the northern BS area, it meets the UHI circulation. The vertical updraft in the front of the sea breeze merges with the rising branch of the UHI circulation. Once the rising air is above the boundary layer, the air flows from the land to the sea driven by the horizontal pressure gradient, then sinks to form a complete secondary SBC. In addition, the enhancement of the sea breeze and urban surface temperature increase the instability of the near surface atmosphere, which can strengthen the convergence updraft caused by the SBF. The larger roughness and drag of the city slow the advancing SBF, strengthening the convergence of the horizontal wind field, and further increasing the vertical velocity of the updraft. A well-developed, clockwise SBC (at ~31.4°N) lasts for 2-3 hours, extending ~6-7 km horizontally and nearly 1 km vertically.

In addition, figure 13b-d show the dryer island with light purple (9-13 g $kg^{-1}$ in color bar) at 31.3°N nearby than surroundings. Areas with low humidity located where strong downward motions occur transport drier cooler air from aloft to the surface, thus decreasing the column specific humidity. The high humidity associated with the sea breeze penetrates inland ~2 km at the northern coastal suburb but ~4 km at the southern coastal exurban area because of both the urban morphology and the maritime area.

In the evening (2000 LST; Fig. 12f, 13f), the land surface cools more quickly than the sea and the sea-breeze circulation dissipates gradually. The synoptic wind causes the inconspicuous land-breeze circulation through the night to the early morning. The specific humidity differences are reduced after sunset with the limited evaporation over both urban and exurban areas. As the vertical motions weaken after sunset, an inland upper-level nocturnal wet layer forms probably associated with the warmer air and with higher vapor pressures with less condensation above the urban area (cf. exurban). The entire atmosphere returns to being thermodynamically stable.

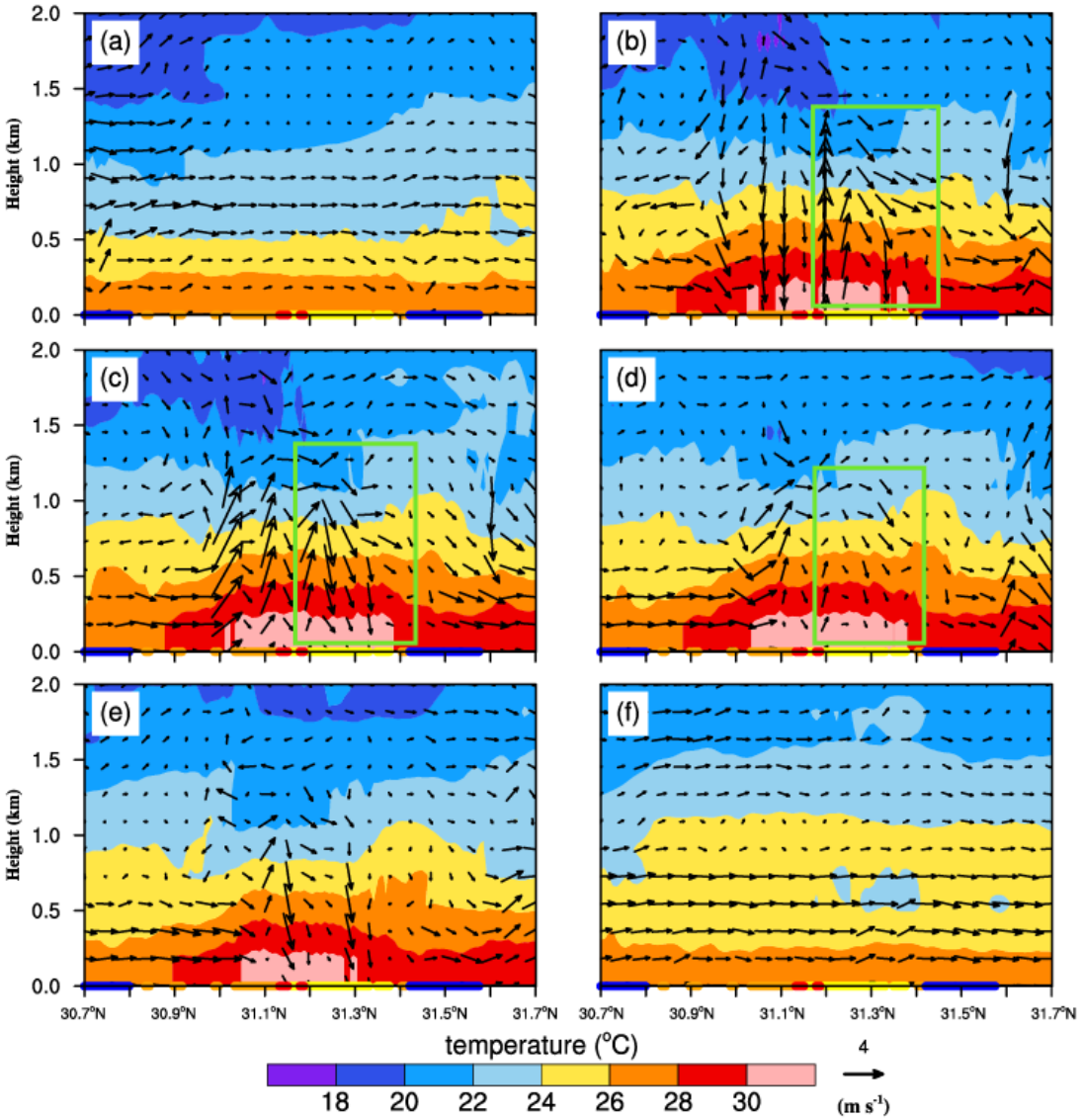


**Figure 12**: Cross section (transect A-B, Fig. 1b) of wind (vectors; v component-w ×10 scale) and air temperature (°C) on 13 August 2016 at (a) 08:00, (b) 12:00, (c) 13:00, (d) 14:00, (e) 15:00, (f) 20:00. Land-use of each grid (lower X axis, colors defined as Fig. 1c, d) and urban circulations in Shanghai (green boxes) are shown.

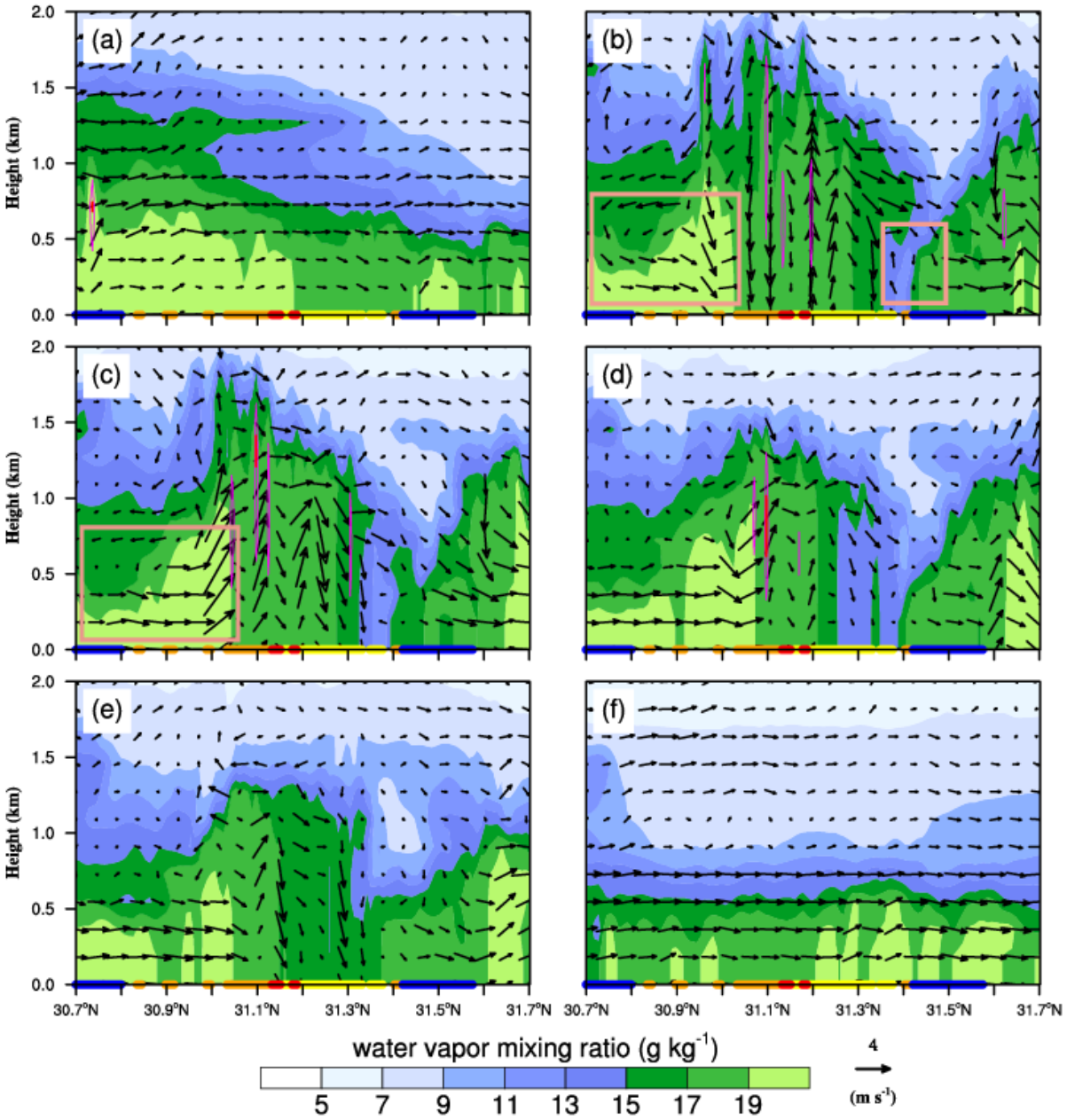


**Figure 13**: As Fig.12, but cross section of mixing ratio (g kg$^{-1}$; key), vertical velocity (m s$^{-1}$) with 1.0 (purple), and 1.5 (red) m s$^{-1}$ contours and sea breeze circulations in Shanghai (pink boxes).

### *4.4 Boundary layer structure*

The vertical advection of potential temperature ($-w\,\partial\theta/\partial z$; where $w$ is the vertical velocity, $\theta$ potential temperature, and $z$ vertical coordinate) in the thermodynamic energy equation is evaluated at three sites. On 12$^{th}$ August, above the urban XJH area subsidence heating is evident in the morning above the boundary layer. During the afternoon of the 13$^{th}$ August it is large (Fig. 13a). This subsidence heating contributes to increasing the air temperature in the urban area, with larger values at XJH than at BS or FX (Fig. 13b, c). This implies stronger heating associated with the stronger urban circulation may be responsible for a larger temperature anomaly. Thus, the larger sensible heat flux, the resulting UHI, and the subsidence heating all play an important role in increasing the air temperature and causing the potential temperature to decrease with height at urban. With this the atmosphere above the city will be unstable and tend to rise in the afternoon.

During the day, this larger urban heating (cf. surroundings) makes the mixing and the boundary layer entrainment greater, resulting in a deeper urban planetary boundary layer (PBL) than the exurban areas. The top of the modeled PBL reaches ~1.3 km (XJH; at 1400 LST, Fig. 13a), but is only ~0.5 km over suburbs (BS; Fig. 13b) and nearly 0.9 km over exurban (FX; Fig. 13c). Therefore, the urban diurnal variation of PBL is greater than its surroundings. The PBL height of suburban (BS) is lower than exurban (FX), which might because BS is nearer the sea than FX and located upwind of the sea breeze.

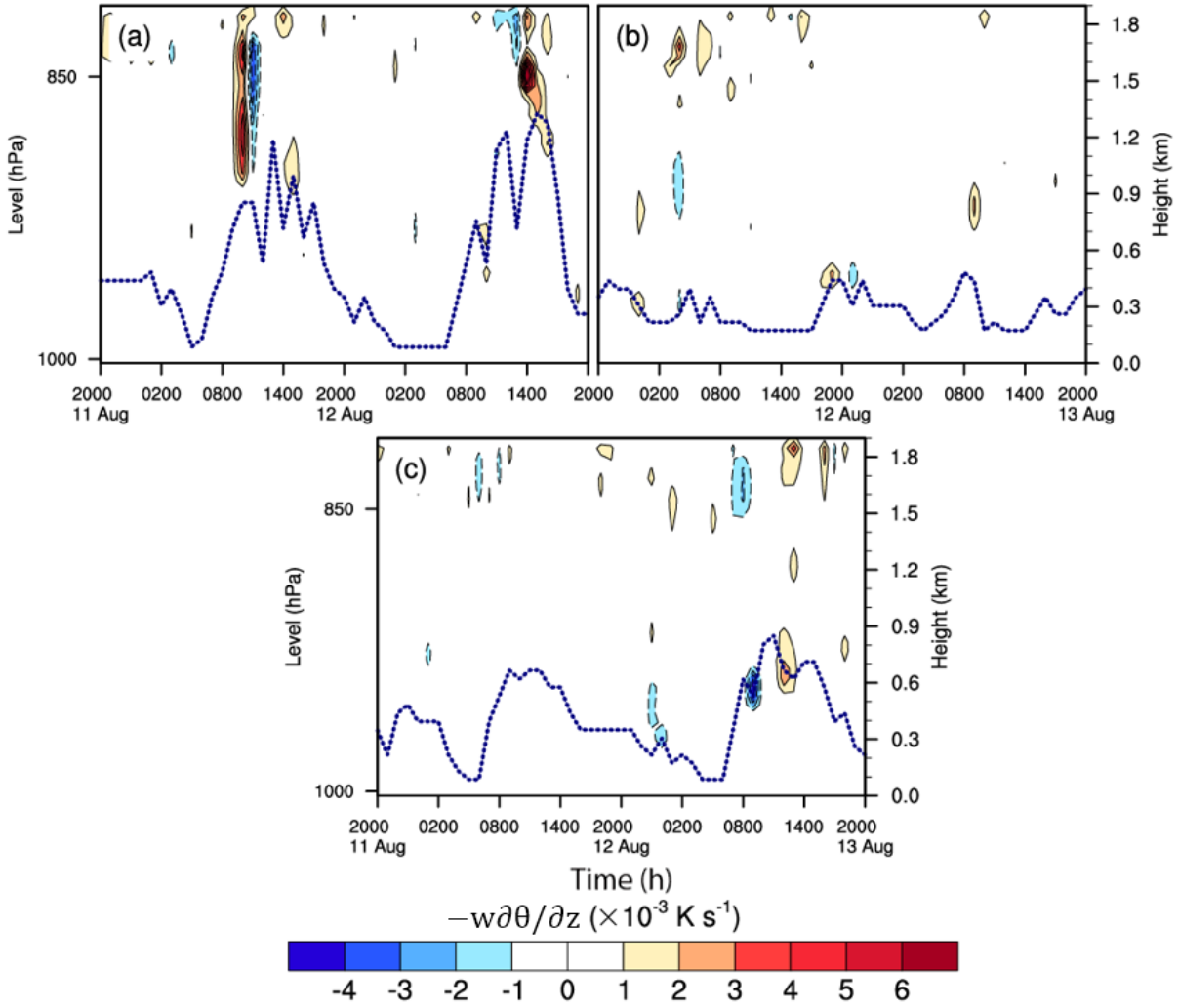


**Figure 14**: Simulated vertical advection of potential temperature ($-w\,\partial\theta/\partial z$) and planetary boundary layer height (blue lines) in the period from 20:00 11th to 20:00 13th August 2016 over: (a) XJH, (b) BS, and (c) FX.

## 5. Conclusions

An urban heat island (UHI) - sea breeze circulation (SBC) study is undertaken in the Shanghai area used a mesoscale model (WRF) with an urban scheme (SLUCM) informed by MODIS and local surface information, including parameters derived for one urban class (high-intensity residential, HIR) using local flux observations.

Evaluation using HIR area flux observations demonstrate the model can reproduce SEB fluxes reasonably. Consistent with other studies, incoming shortwave is systematically overestimated, but compensating the errors which result in better performance for net all wave radiation (MBE = +27 W $m^{-2}$, or better when the local-scale SEB fluxes are assessed: MBE = +16 W $m^{-2}$). Overall, $Q_H$ is underestimated. Evaluation of the canopy layer meteorology at three sites across Shanghai suggests both 2-m air temperature and humidity are underestimated especially at night, which can be explained by the underestimated $Q_F$ and $Q_E$. Overall, the model performs best in south central Shanghai. Based on these results we conclude that the model can be used to explore the interaction between UHI and SBC but recognize the model improvements would probably of interest being stronger.

From observations, the sea breeze develops in the northern coastal suburb of Shanghai. It is accompanied with changes of wind direction and increases of wind velocity. Results from this study show that the model can simulate the evolution of the sea breeze within the background wind field. The sea breeze on 13 August 2016 lasts for 4 hours and is strongest at 1200-1400 LST (maximum height of nearly 1.0 km) and declines at 1600 LST. The observed (modeled) maximum UHI is 3.5°C (2.7°C) in the afternoon. The maximum UHI drifts northwest in the afternoon with the prevailing southeast wind. The subsidence heating contributes to the increasing of air temperature in the urban area and the urban diurnal variation of PBL (maximum height: ~1.3 km) is greater than its surroundings.

The sea breeze and urban circulations can be characterized as follows:

- An urban circulation (horizontal/vertical/time period scale: ~20 km/ ~1.5 km/ ~3-h) with thermal vertical motions (~1.5 m $s^{-1}$) above the urban area and a SBC (horizontal/vertical/time period scale: 6 - 7 km/ ~1 km/ 2 - 3-h) above the northern coastal suburb occur.
- Combined the sea breeze and southerly winds form a low-level wind shear (convergence zone) ~5 km from the coast that penetrates ~20 km inland to the urban center.
- The southern coastal sea breeze penetrates inland faster than the northern coastal.

- The low-level convergence, vertical motion and moisture transport that result from the sea and urban breeze are crucial for the modification of the urban atmospheric environment.
- Low-level moisture is transported from the sea to ~2 (in the north) - 4 (south) km inland.
- The atmosphere affected by the UHI and sea breeze over the urban is unstable, with vertical upward motion in the afternoon.
- Observed and simulated regional wind speed and dominant wind direction differences are small except at the southern boundary of the model domain.

This study suggests that better representation of urban surface morphology (e.g., plan area fraction buildings, plan area fraction paved, building height, and roof width) and material properties (e.g., surface albedo, heat capacity, thermal conductivity, and surface emissivity) are key to improving simulated urban land surface forcing and associated circulations on local meteorological conditions. These require detailed observations and parameterizations (e.g., meteorological, land cover).

We note some limitations in this work. First, although we have considered some local urban thermal parameters, numerous complex effects (dynamic parameters: urban surface roughness; optimized thermal dynamic parameters of other various surface categories) remain to be considered. Second, we use WRF/SLUCM with other commonly selected model physics, these could be much more broadly explored . Third, assessing if use of other urban canopy models (e.g., BEP/BEM: Martilli 2002; Chen et al. 2011a; TEB: Meyer et al. 2020) or more improved local SLUCM parameters is the more critical to improving model performance would be useful to assess over a broader number of case studies.

This study demonstrates the value of WRF/SLUCM simulations in understanding the complex spatial dynamics of summer-time urban heating in coastal megacities such as Shanghai. Interactions among the local circulations will differ with weather conditions. Hence, future studies should quantify the effects of parameterization schemes and morphological parameters within urban canopy models. For example, to consider local strong convective storms, heavy rainfall induced by UHI and sea breeze meteorological conditions. Improving land cover and anthropogenic heat flux data would all be beneficial. Clearly, a longer simulation time would allow more extensive analysis of the large-scale climatic effects caused by urbanization in and around the megacity of Shanghai.

**Acknowledgments**

This research was joint funded by the National Natural Science Foundation of China (grant number 41775019, 41275021), China Special Fund for Meteorological Research in the Public Interest (grant number GYHY201306023), the UK-China Research & Innovation Partnership Fund through the Met Office Climate Science for Service Partnership (CSSP) China as part of the Newton Fund (SG), the Social Development Project of Shanghai Municipal Science and Technology Innovation Action Plan (No. 19DZ1203400), and the Research Program from Science and Technology Committee of Shanghai (No. 21ZR1457700).

## REFERENCES

Allen, L., F. Lindberg, and C. S. B. Grimmond, 2011: Global to city scale urban anthropogenic heat flux: Model and variability. *Int. J. Climatol*., **31**, 1990–2005, https://doi.org/10.1002/joc.2210.

Ao, X., and Coauthors, 2016a: Heat, water and carbon exchanges in the tall megacity of Shanghai: Challenges and results. *Int. J. Climatol*., **36**, 4608–4624, https://doi.org/10.1002/joc.4657.

Ao, X., C. S. B. Grimmond, D. Liu, Z. Han, P. Hu, Y. Wang, X. Zhen, and J. Tan, 2016b: Radiation fluxes in a business district of Shanghai, China. *J. Appl. Meteor. Climatol*., **55**, 2451–2468, https://doi.org/10.1175/JAMC-D-16-0082.1.

Ao, X., and Coauthors, 2018: Evaluation of the surface urban energy and water balance scheme (SUEWS) at a dense urban site in Shanghai: Sensitivity to anthropogenic heat and irrigation. *J. Hydrometeor.*, **19**, 1983–2005, https://doi.org/10.1175/JHM-D-18-0057.1.

Ao, X., and Coauthors, 2019a: Synergistic interaction between urban heat island and heat waves and its impact factors in Shanghai. *Acta. Geogr. Sinica.* **74**:1789-1802, DOI: 10.11821/dlxb201909007. (in Chinese).

Ao, X., and Coauthors, 2019b: Observed Synergies between Urban Heat Islands and Heat Waves and Their Controlling Factors in Shanghai, China, *J. Appl. Meteor. Climatol.*, **58**, 1955-1972.

Bornstein, R. D., and D. S. Johnson, 1977: Urban-rural wind velocity differences. *Atmos. Environ*., **11**, 597–604, doi: 10.1016/0004-6981(77)90112-3.

Best. M.J., and C.S.B. Grimmond, 2015: Key conclusions of the First International Urban Land Surface Model Comparison Project. *Bull. Amer. Meteor. Soc.,* 96, 805–819, https://doi.org/10.1175/BAMS-D-14-00122.1.

Block, A., K. Keuler, and E. Schaller, 2004: Impacts of anthropogenic heat on regional climate patterns. *Geophys. Res. Lett.*, **31**, L12211, https://doi.org/10.1029/2004GL019852.

Chen, F., and J. Dudhia, 2001: Coupling an advanced land surface hydrology model with the Penn State–NCAR MM5 modeling system. Part I: Model implementation and sensitivity. *Mon. Wea. Rev*., **129**, 569-585.

Chen, F., and Coauthors, 2011a: The integrated WRF/urban modeling system: Development, evaluation, and applications to urban environmental problems. *Int. J. Climatol*., **31**, 273–288, https://doi.org/10.1002/joc.2158.

Chen, F., S. Miao, M. Tewari, J. Bao, and H. Kusaka, 2011b: A numerical study of interactions between surface forcing and sea breeze circulations and their effects on stagnation in the greater Houston area. *J. Geophys. Res*., **116**, D12105, https://doi.org/10.1029/2010JD015533.

Cheng, F., and D. W. Byun, 2008: Application of high resolution and use and land cover data for atmospheric modeling in the Houston–Galveston metropolitan area. Part I: Meteorological simulation results. *Atmos. Environ*., **42**, 7795-7811, https://doi.org/10.1016/j.atmosenv.2008.04.055.

Childs, P.P., S, Raman, 2005: Observations and numerical simulations of urban heat island and sea breeze circulations over New York City. *Pure Appl. Geophys*., **162**, 1955-1980.

Cohen, W. B., and Coauthors, 2006: MODIS land cover and LAI collection 4 product quality across nine states in the western hemisphere. *IEEE Transactions on Geoscience & Remote Sensing*, **44**, 1843-1857.

Crosman, E. T. and J. D. Horel, 2010: Sea and lake breezes: a review of numerical studies. *Bound.-Layer Meteor.*, **137**, 1-29.

Dandou, A., M. Tombrou, and N. Soulakellis, 2009: The influence of the city of Athens on the evolution of the sea-breeze front. *Bound.-Layer Meteor.*, **131**, 35-51, https://doi.org/10.1007/s10546-008-9306-x.

Dou, J.J., Y.C. Wang, R. D. Bornstein, and S.G. Miao, 2015: Observed spatial characteristics of Beijing urban climate impacts on summer

thunderstorms. *J. Appl. Meteor. Climatol*., **54**, 94-104.

Ek, M. B., K. E. Mitchell, Y. Lin, E. Rogers, P. Grunmann, V. Koren, G. Gayno, and J. D. Tarpley, 2003: Implementation of Noah land surface model advances in the National Centers for Environmental Prediction operational mesoscale Eta model. *J. Geophys. Res*., **108**, 8851, https://doi.org/10.1029/2002JD003296.

Feudo, T. L., and Coauthors, 2015: Comparison of hourly solar radiation from a ground–based station, remote sensing and weather forecast models at a coastal site of South Italy (Lamezia Terme). *Energy Procedia. Elsevier*, **76**, 148–155. https://doi.org/10.1016/j.egypro.2015.07.884.

Freitas, E.D., C.M. Rozoff, W.R. Cotton, and P.L.S. Dias, 2007: Interactions of an urban heat island and sea-breeze circulations during winter over the metropolitan area of São Paulo, Brazil. *Bound.-Layer Meteor*., **122**, 43-65, https://doi.org/10.1007/s10546-006-9091-3.

Gabey, A. M., C. S. B. Grimmond, and I. Capel-Timms, 2018: Anthropogenic heat flux: Advisable spatial resolutions when input data are scarce. *Theor. Appl. Climatol*., **135**, 791-807, https://doi.org/10.1007/s00704-018-2367-y.

Garratt, J. R., 1994: The Atmospheric Boundary Layer, Cambridge Univ. Press, New York, 49-60.

Giovannini, L., D. Zardi, M. de Franceschi, and F. Chen, 2014: Numerical simulations of boundary–layer processes and urban–induced alterations in an Alpine valley. *Int. J. Climatol.*, **34**, 1111-1131.

Garratt J.R., 1990: The internal boundary layer—a review. *Bound.-Layer Meteor.*, **50**,171–203.

Grimmond, C.S.B., T.R. Oke, and H.A. Cleugh, 1993: The role of "rural" in comparisons of observed suburban - rural flux differences. Exchange processes at the land surface for a range of space & time scales. *Inter. Association of Hydrological Sciences Publication*, **212**, 165-174.

Grimmond, C.S.B. and Coauthors, 2010: The international Urban Energy Balance Models Comparison Project: First results from phase 1. *J. Appl. Meteor. Climatol.*, **49**, 1268–1292, https://doi.org/10.1175/2010JAMC2354.1.

Grimmond, C.S.B. and Coauthors, 2011: Initial results from phase 2 of the International Urban Energy Balance Model Comparison. *Int.J. Climatol.*, **31**, 244–272.

Grimmond, C.S.B. and Coauthors, 2020: Integrated urban hydrometeorological, climate and environmental services: concept, methodology and key messages. *Urban Clim.*, **33**, 2212–0955.

Grimmond C.S.B. and H.C. Ward, 2021: Urban Observations T. Foken (Ed.), *Springer Handbook of Atmospheric Measurements, Springer Handbooks*, https://doi.org/10.1007/978-3-030-52171-4_52, 1397-1429.

Gu, W., J. Zhang, J. Tan, J. Dai, and C. Yue, 2017: Characteristics and circulation background of Shanghai summer sea breeze front and its induced convection. *J. Trop. Meteor*., **33**, 644-653, https://doi.org/10.16032/j.issn.1004-4965.2017.05.008. (in Chinese)

Gutiérrez, E., J.E. Gonzalez, A. Martilli, and R. Bornstein, 2015: On the anthropogenic heat fluxes using an air conditioning evaporative cooling parameterization for mesoscale urban canopy models. *J. Sol. Energy Eng*., **137,** doi: 10.1115/1.4030854.

Hong, S., and J. Lim, 2006: The WRF single-moment 6-class microphysics scheme (WSM6). *J. Korean Meteor. Soc*., **42**, 129-151.

Iacono, M. J., J. S. Delamere, E. J. Mlawer, M. W. Shephard, S. A. Clough, and W. D. Collins, 2008: Radiative forcing by long-lived greenhouse gases: Calculations with the AER radiative transfer models. *J. Geophys. Res*., **113**, D13103, https://doi.org/10.1029/2008JD009944.

Janjić, Z.I., 1994: The step-mountain Eta coordinate model: Further developments of the convection, viscous sublayer, and turbulence closure schemes. *Mon. Wea. Rev*., **122**, 927-945.

Jiang, S., X. Lee, J. Wang, and K. Wang, 2019: Amplified urban heat islands during heat wave periods. *J. Geophys. Res.: Atmospheres*, **124**, 7797–7812, https://doi.org/10.1029/2018JD030230.

Keeler, J. M., and D. A. R. Kristovich, 2012: Observations of urban heat island influence on lake-breeze frontal movement. *J. Appl. Meteor. Climatol*., **51**, 702–710, doi:10.1175/JAMC-D-11-0166.1.

Kent C., and Coauthors, 2017: Evaluation of urban local-scale aerodynamic parameters: implications for the vertical profile of wind speed and for source areas. *Bound.-Layer Meteor.*, **164**:183–213.

Kusaka, H., H. Kondo, Y. Kikegawa, and F. Kimura, 2001: A simple single-layer urban canopy model for atmospheric models: Comparison with multi-layer and slab models. *Bound.-Layer Meteor.*, **101**, 329-358.

Kusaka, H., and F. Kimura, 2004: Coupling a single-layer urban canopy model with a simple atmospheric model: Impact on urban heat island simulation for an idealized case. *J. Meteor. Soc. Japan*, **82**, 67-80.

Lee S.H., and Coauthors, 2011: Evaluation of urban surface parameterizations in the WRF model using measurements during the Texas Air Quality Study 2006 field campaign. *Atmos. Chem. Phys*., **11**, 2127-2143.

Leroyer S., and Coauthors, 2014: Subkilometer numerical weather prediction in an urban coastal area: a case study over the vancouver metropolitan area. *J. Appl. Meteor. Climatol*., **53**, 1433-1453.

Loridan, T., and Coauthors, 2010: Trade-offs and responsiveness of the single-layer urban canopy parameterization in WRF: An offline evaluation using the MOSCEM optimization algorithm and field observations. *Quart. J. Roy. Meteor. Soc.*, **136**, 997-1019.

Loridan, T., F. Lindberg, O. Jorba, S. Kotthaus, S. Grossman-Clarke, and C. S. B. Grimmond, 2013: High resolution simulation of surface heat flux variability across central London with urban zones for energy partitioning. *Bound.-Layer Meteor*., **147**, 493–523, https://doi.org/10.1007/s10546-013-9797-y.

Lee S.H., and Coauthors, 2011: Evaluation of urban surface parameterizations in the WRF model using measurements during the Texas Air Quality Study 2006 field campaign. *Atmos. Chem. Phys*., **11**, 2127-2143.

Li, D., E. Bou-Zeid, M. L. Baeck, S. Jessup, and J. A. Smith, 2013a: Modeling land surface processes and heavy rainfall in urban environments: Sensitivity to urban surface representations. *J. Hydrometeor*., **14**, 1098–1118, https://doi.org/10.1175/JHM-D-12-0154.1.

Li, D., E. Bou-Zeid, M. Barlage, F. Chen, and J. A. Smith, 2013b: Development and evaluation of a mosaic approach in the WRF-Noah framework. *J. Geophys. Res. Atmos.*, **118**, 11918-11935.

Li, D., and E. Bou-Zeid, 2013c: Synergistic interactions between urban heat islands and heat waves: The impact in cities is larger than the sum of its parts. *J. Appl. Meteor. Climatol.*, **52**, 2051-2064.

Li, D., and E. Bou-Zeid, 2014: Quality and sensitivity of high‐resolution numerical simulation of urban heat islands. *Environ. Res. Lett.* IOP Publishing, 9(5).

Li, D., J. Shu, and J. Tan, 2015a: A numerical simulation experiment of an urban summer heat wave based on modified data of land-use and anthropogenic heat. *J. Trop. Meteorol.*, **31**, 364-373. (in Chinese)

Li, D., and Coauthors, 2015b: Contrasting responses of urban and rural surface energy budgets to heat waves explain synergies between urban heat islands and heat waves. *Environ. Res. Lett.*, **10**, 054009.

Li, D., and Coauthors, 2016: Changes in wind speed under heat waves enhance urban heat islands in the Beijing metropolitan area, *J. Appl. Meteor. Climatol.*, **55**, 2369-2375.

Li, M., T. Wang, M. Xie, B. Zhuang, S. Li, Y. Han, and N. Cheng, 2017: Modeling of urban heat island and its impacts on thermal circulations in the Beijing-Tianjin-Hebei region, China. *Theor. Appl. Climatol*., **128**, 999-1013.

Lindberg, F., C.S.B. Grimmond, N. Yogeswaran, S. Kotthaus, and L. Allen, 2013: Impact of city changes and weather on anthropogenic heat flux in Europe 1995-2015. *Urban Clim.*, **4**, 1-15.

Liu, D., and Coauthors, 2018: A new model to downscale urban and rural surface and air temperatures evaluated in Shanghai, China. *J. Appl. Meteor. Climatol*., **57**, 2267–2283, https://doi.org/10.1175/JAMC-D-17-0255.1.

Martilli, A., 2002: Numerical study of urban impact on boundary layer structure: Sensitivity to wind speed, urban morphology, and rural soil moisture. *J. Appl. Meteor. Climatol*., **41**, 1247 – 1266. https://doi.org/10.1175/1520-0450 (2002)041<1247: NSOUIO>2.0.CO; 2

Meyer D, R Schoetter, Maik Riechert, Antoine Verrell, M Tewari, J Dudhia, V Masson, M van Reeuwijk, S Grimmond 2020: WRF-TEB: implementation and evaluation of the coupled Weather Research and Forecasting (WRF) and Town Energy Balance (TEB) model *Journal of Advances in Modeling Earth Systems* 12 (8) e2019MS001961 https://doi.org/10.1029/2019MS001961

Mlawer, E. J., S. J. Taubman, P. D. Brown, M. J. Iacono, and S. A. Clough, 1997: Radiative transfer for inhomogeneous atmospheres: RRTM, a validated correlated-k model for the longwave, *J. Geophys. Res.*, **102**, 16 663-16 682.

Miao, S., F. Chen, M. A. Lemone, M. Tewari, Q. Li, and Y. Wang, 2009: An observational and modeling study of characteristics of urban heat island and boundary layer structures in Beijing. *J. Appl. Meteor. Climatol*., **48**, 484-501, https://doi.org/10.1175/2008JAMC1909.1.

Miller, S. T., B. D. Keim, R. Talbot, and H. Mao, 2003: Sea breeze: Structure, forecasting, and impacts. *Reviews of Geophysics*, **41**, 1-31.

MODIS, 2017: MODIS land cover type/dynamics page, accessed 1 June 2018, http://modis.gsfc.nasa.gov/data/dataprod/mod12.php

Monin, A. S., and A. M. Obukhov, 1954: Basic laws of turbulent mixing in the surface layer of the atmosphere. *Tr. Geofiz. Inst., Akad. Nauk SSSR*, **24**, 163-187.

Narumi, D., A. Kondo, and Y. Shimoda, 2009: Effects of anthropogenic heat release upon the urban climate in a Japanese megacity. *Environ. Res.*, **109**, 421-431.

NOAA, 2017: NCEP SST Analysis Page, accessed 1 July 2017, http://polar.ncep.noaa.gov/pub/history/sst.

Ohashi, Y., and H. Kida, 2002: Effects of mountains and urban areas on daytime local-circulations in the Osaka and Kyoto regions. *J. Meteor. Soc. Japan*, **80**, 539-560.

Oke, T. R., 1978: *Boundary Layer Climates*. Routledge, 435 pp.

Oke, T. R., 1981: Canopy geometry and nocturnal urban heat island: comparison of scale model and field observations. *J. Climatol*., **1**, 237-254.

Oke, T. R., G. Mills, A. Christen, and J. A. Voogt, 2017: Urban climates. Cambridge: Cambridge University Press. https://doi.org/10.1017/9781139016476.

Pitman, A. J. T., 1994: Assessing the sensitivity of a land-surface scheme to the parameter values using a single column model. *J. Climate*, **7**, 1856-1869, doi.org/10.1175/1520-0442 (1994)007, 1856:ATSOAL.2.0.CO; 2.

RDA, 2017: Research Data Archive, accessed on 1 July 2017, http://rda.ucar.edu/datasets/ds083.2/

Roberts, S. M., T. R. Oke, C. S. B. Grimmond, and J. A. Voogt, 2006: Comparison of four methods to estimate urban heat storage. *J. Appl. Meteor. Climatol*., **45**, 1766–1781, https://doi.org/10.1175/JAM2432.1.

Roth, M., and T. R. Oke, 1994: Comparison of modelled and "measured heat storage in suburban terrain." *Contributions to Atmospheric Physics*, **67**, 149–156.

Ruiz-Arias, J. A., C. Arbizu-Barrena, F. J. Santos-Alamillos, J. Tovar-Pescador, and D. Pozo-Vázquez, 2016: Assessing the surface solar radiation budget in the WRF model: A spatiotemporal analysis of the bias and its causes, *Mon. Wea. Rev.*, **144**, 703-711, https://doi.org/10.1175/MWR-D-15-0262.1.

Ryu YH, JJ Baik, 2013: Daytime local circulations and their interactions in the Seoul metropolitan area. *J. Appl. Meteor. Climatol.*, **52**, 784-801.

Sailor, D. J., 2011: A review of methods for estimating anthropogenic heat and moisture emissions in the urban environment. *Int. J. Climatol.*, **31**, 189–199, https://doi.org/10.1002/joc.2106.

Salamanca, F., A. Martilli, M. Tewari, and F. Chen, 2011: A study of the urban boundary layer using different urban parameterizations and high-resolution urban canopy parameters with WRF. *J. Appl. Meteorol. Climatol*., **50**, 1107-1128.

Shen, Z., J. Shi, J. Tan, and H. Yang, 2020: The migration of the warming center and urban heat island effect in Shanghai during urbanization. *Front. Earth Sci*., **8**, 340. https://doi.org/10.3389/feart.2020.00340.

Shin, H. H., and S. Y. Hong, 2011: Intercomparison of Planetary Boundary-Layer Parametrizations in the WRF Model for a Single Day from CASES-99. *Bound.-Layer Meteor.*, **139**, 261-281.

Stewart, I. D., and T. R. Oke, 2012: ''Local climate zones'' for urban temperatures studies. *Bull. Amer. Meteor. Soc.*, **93**, 1879–1900, doi:10.1175/BAMS-D-11-00019.1.

Strassberg, D., M. A. LeMone, T. T. Warner, and J. G. Alfieri, 2008: Comparison of Observed 10-m Wind Speeds to Those Based on Monin–Obukhov Similarity Theory Using IHOP_2002 Aircraft and Surface Data, *Monthly Weather Review*, **136**, 964-972.

Sun, J., and P. Hu, 2009: Study on real time quality control system of Shanghai automatic weather station. *Meteorological, Hydrological and Marine Instruments*, **4**, 38-41. (in Chinese)

Su, Z., X. Zhi, J. Bian, R. Li, and J. Sun, 2014: Research on the influence of precipitation on traffic characteristics of urban expressway in Shanghai. *Atmos. Sci. Res. Appl*., **1**, 68-76. (in Chinese)

Tan, J. G., and Coauthors, 2010: The urban heat island and its impact on heat waves and human health in Shanghai. *Int. J. Biometeor*., **54**, 75–84, https://doi.org/10.1007/s00484-009-0256-x.

Tan, J. G., and Coauthors, 2015: Urban Integrated Meteorological Observations: Practice and Experience in Shanghai, China. *Bull. Amer. Meteor. Soc*., **96**, 85-102.

Theeuwes N.E., and Coauthors, 2019: Parameterizing horizontally averaged wind and temperature profiles in the urban roughness sublayer. *Bound.-Layer Meteor.*, **173**, 321–348, https://doi.org/10.1007/s10546-019-00472-1.

Thompson, W.T., T. Holt, and J. Pullen, 2007: Investigation of a sea breeze front in an urban environment. *Quart. J. Roy. Meteor. Soc.*, **133**, 579-594.

Tsiringakis A., and Coauthors, 2019: On- and off-line evaluation of the single-layer urban canopy model in London summertime conditions. *Q J R Meteorol Soc*. **145**, 1474–1489. https://doi.org/10.1002/qj.3505.

Varquez, A. C., M. Nakayoshi, and M. Kanda, 2015: The Effects of Highly Detailed Urban Roughness Parameters on a Sea-Breeze Numerical Simulation. *Bound.-Layer Meteor.*, **154**, 449-469. https://doi.org/10.1007/s10546-014-9985-4.

Wang, Y., and Coauthors, 2017: Impact of land surface heterogeneity on urban heat island circulation and sea‐land breeze circulation in Hong Kong, *J. Geophys. Res. Atmos*., **122**, 4332 – 4352, doi: 10.1002/2017JD026702.

Wang, Z.-H., Bou-Zeid, E., Au, S. and Smith, J., 2011: Analyzing the sensitivity of WRF's single-layer urban canopy model to parameter uncertainty using advanced Monte Carlo simulation. *J. Appl. Meteorol. Climatol*., **50**, 1795–1814.

WMO 2021, WMO Guidance on the Canopy Layer Urban Heat Island (in prep.).https://community.wmo.int/activity-areas/urban/urban-heat-island.

Yoshikado, H., 1990: Vertical structure of the sea breeze penetrating through a large urban complex. *J. Appl. Meteor.*, **29**, 878-891.

Yoshikado, H., 1992: Numerical study of the daytime urban effect and its interaction with the sea breeze. *J. Appl. Meteor*., **31**, 1146-1164.

You, C., Chi-Hung Fung, J., and Tse, W. P., 2019: Response of the Sea Breeze to Urbanization in the Pearl River Delta Region, *J. Appl. Meteorol. Climatol*., **58**, 1449-1463.

Zhao, W., N. Zhang, J. Sun, and J. Zou, 2014a: Evaluation and parameter-sensitivity study of a single-layer urban canopy model (SLUCM) with measurements in Nanjing, China. *J. Hydrometeor*., **15**, 1078-1090.

Zhao, L., X. Lee, R. B. Smith, and K. Oleson, 2014b: Strong contributions of local background climate to urban heat islands. *Nature*, **511**, 216–219, doi: 10.1038/nature13462.